FIBROSIS

An aging bone marrow exacerbates lung fibrosis by fueling profibrotic macrophage persistence

Asma Farhat[1,2], Mariem Radhouani[1,2], Florian Deckert[1,2], Sophie Zahalka[1,2], Lisabeth Pimenov[1], Alina Fokina[1], Anna Hakobyan[2,3,4], Felicitas Oberndorfer[5], Jessica Brösamlen[1], Anastasiya Hladik[1], Karin Lakovits[1], Fanzhe Meng[1], Federica Quattrone[1,2], Louis Boon[6], Cornelia Vesely[7], Philipp Starkl[1], Nicole Boucheron[8], Jörg Menche[2,3,4,9,10], Joris van der Veeken[11], Wilfried Ellmeier[8], Anna-Dorothea Gorki[1], Clarissa Campbell[2], Riem Gawish[1]†, Sylvia Knapp[1,12]*†

Pulmonary fibrosis is an incurable disease that manifests with advanced age. Yet, how hematopoietic aging influences immune responses and fibrosis progression remains unclear. Using heterochronic bone marrow transplant mouse models, we found that an aged bone marrow exacerbates lung fibrosis irrespective of lung tissue age. Upon lung injury, there was an increased accumulation of monocyte-derived alveolar macrophages (Mo-AMs) driven by cell-intrinsic hematopoietic aging. These Mo-AMs exhibited an enhanced profibrotic profile and stalled maturation into a homeostatic, tissue-resident phenotype. This delay was shaped by cell-extrinsic environmental signals such as reduced pulmonary interleukin-10 (IL-10), perpetuating a profibrotic macrophage state. We identified regulatory T cells (T_{regs}) as critical providers of IL-10 upon lung injury that promote Mo-AM maturation and attenuate fibrosis progression. Our study highlights the impact of an aging bone marrow on lung immune regulation and identifies T_{reg}-mediated IL-10 signaling as a promising target to mitigate fibrosis and promote tissue repair.

INTRODUCTION

With rising life expectancies and a growing aging population, understanding how advanced age leads to increased disease morbidity is an imminent public health concern (*1*). Aging is associated with enhanced vulnerability to chronic respiratory pathologies, including idiopathic pulmonary fibrosis (IPF) (*2*, *3*). IPF is characterized by progressive and severe scarring of the lung tissue, ultimately leading to lung failure (*4*). Although genetic predisposition and environmental triggers contribute to its etiology, advanced age is by far the most prevalent risk factor for onset of the disease (*5*). Age-related cellular senescence, aberrant epithelial activation, mitochondrial dysfunction, and impairments in immunity influence IPF disease progression (*6*–*8*). Repair and regeneration are vital for maintaining tissue integrity (*9*), with tissue-resident (TR) alveolar macrophages (AMs) playing a key role in preserving lung homeostasis during early life. Homeostatic TR-AMs self-renew with minimal contribution from circulating monocytes (*10*, *11*). Damage to the alveolar epithelium during severe lung inflammation, such as that caused by bleomycin injury, depletes TR-AMs and leads to monocyte recruitment from the bone marrow, which then differentiate into monocyte-derived AMs (Mo-AMs) (*12*–*14*). Although Mo-AMs are beneficial during acute infections (*12*), their chronic presence contributes to pathologies like lung fibrosis (*15*–*17*) given that they secrete profibrotic factors, which activate fibroblasts and sustain the fibrotic process (*18*, *19*). In the lungs, Mo-AMs undergo marked phenotypic and functional changes, eventually acquiring a phenotype similar to that of TR-AMs (*20*–*22*). The speed at which activated Mo-AMs transition into a less reactive TR-AM state contributes to disease outcome and the likelihood of restored lung homeostasis (*23*).

Although previous studies have comprehensively addressed the role of aging lung tissue (*24*) and shown that an increased susceptibility to lung fibrosis with age is associated with elevated Mo-AMs, these effects have been primarily attributed to impairments in epithelial cell proteostasis and differentiation (*20*, *25*). How the aging bone marrow and derived hematopoietic immune cells (i.e., Mo-AMs) affect disease when recruited into a distant organ remains incompletely understood. An aging immune system is characterized by a state of low-grade, systemic inflammation, termed inflammaging (*26*). Although aged hematopoietic stem cells display a reduced regenerative capacity, intrinsic changes in their differentiation potential and a higher propensity for myelopoiesis lead to an expansion of myeloid progenitors and mature cells at the expense of lymphopoiesis (*27*–*30*). This skewing contributes to an increase in myeloid-based malignancies with age, which coincides with impaired adaptive immunity. Such changes impair the immune system's inability to mount an appropriate immune response or promote tissue integrity and repair (*31*).

In this study, we asked whether immune cells derived from an aged bone marrow could influence inflammation and fibrosis in the lungs. We found that an aged bone marrow autonomously produced more profibrotic Mo-AMs, which propagated fibrosis development independent of pulmonary tissue age. In the lungs, these Mo-AMs were slower to adopt a homeostatic tissue-resident phenotype because

[1]Research Division of Infection Biology, Department of Medicine I, Medical University of Vienna, Vienna, Austria. [2]Research Center for Molecular Medicine of the Austrian Academy of Sciences, CeMM, Vienna, Austria. [3]Max Perutz Labs, Vienna Biocenter Campus (VBC), Vienna, Austria. [4]Department of Structural and Computational Biology, University of Vienna, Vienna, Austria. [5]Department of Pathology, Medical University of Vienna, Vienna, Austria. [6]JJP Biologics, Warsaw, Poland. [7]Center for Anatomy and Cell Biology, Medical University of Vienna, Vienna, Austria. [8]Institute of Immunology, Center for Pathophysiology, Infectiology and Immunology, Medical University of Vienna, Vienna, Austria. [9]Faculty of Mathematics, University of Vienna, Vienna, Austria. [10]Ludwig Boltzmann Institute for Network Medicine at the University of Vienna, Vienna, Austria. [11]Research Institute of Molecular Pathology (IMP), Vienna, Austria. [12]Ignaz Semmelweis Institute, Interuniversity Institute for Infection Research, Vienna, Austria.
*Corresponding author. Email: sylvia.knapp@meduniwien.ac.at
†These authors contributed equally to this work.

of reduced availability of regulatory T cell (T_{reg})–derived interleukin-10 (IL-10), resulting in exacerbated lung fibrosis.

RESULTS

An aged bone marrow exacerbates bleomycin-induced lung fibrosis in mice

Age is a major risk factor for lung fibrosis, as seen in both humans and mice (*2*, *25*). Although dysregulation of the aging epithelia has been described as a prime driver of fibrosis severity, the potential contribution of an aged hematopoietic system remains unclear (*25*). We challenged young-adult (8-week-old) and aged (70-week-old) mice intratracheally with bleomycin to induce fibrosis (Fig. 1A). Aged mice exhibited greater disease severity with sustained body weight loss (Fig. 1B), enhanced collagen deposition (fig. S1A), and increased pulmonary infiltration of myeloid cells, including Mo-AMs (SiglecF^{lo} CD11b^{hi}) (Fig. 1C and fig. S1B; gating strategy in fig. S1C). Given this elevated influx of bone marrow–derived Mo-AMs in aged mice, we asked whether this was driven by changes in the abundance of bone marrow progenitors, considering the age-associated myeloid bias that occurs in the hematopoietic progenitor niche (*30*). At baseline, aged mice had elevated granulocyte-monocyte progenitors (GMPs), reduced common lymphoid progenitors (CLPs) in the bone marrow (fig. S1, D to G), and lower T and B cells in the blood (fig. S1H). By day 7 postbleomycin, aged mice exhibited a pronounced myeloid shift in the bone marrow (Fig. 1D and fig. S1, I and J) and increased neutrophils and monocytes in the blood (fig. S1K). We thus hypothesized that this myeloid skewing in the bone marrow of aged mice could contribute to enhanced recruitment of myeloid cells to the lung and influence the severity of lung fibrosis.

To study the impact of an aging bone marrow independently of structural tissue age, we performed heterochronic bone marrow transplants in which young adult (8-week-old) recipient mice received bone marrow cells from either aged (70-week-old) mice or young adult (8-week-old) controls (Fig. 1E). Two months posttransplantation, we treated mice with bleomycin and analyzed the lungs at 7 days (D7, inflammatory phase) and 14 or 21 days (D14/D21, fibrotic phase) (*15*) postchallenge (Fig. 1E). Young recipient mice transplanted with aged bone marrow showed increased lethality at a dose of 1.5 U/kg (Fig. 1F) and consistently lost more body weight when treated with a lower bleomycin dose (1 U/kg) to ensure survival (Fig. 1G) as compared with control mice that received bone marrow from young donors. Despite both groups having similar, young structural cells in the lungs, including collagen producing fibroblasts (*32*), reconstitution with aged bone marrow increased fibrotic burden. This was evidenced by increased lung collagen deposition (Fig. 1H) and elevated alpha–smooth muscle actin (α-SMA) expression, indicating enhanced myofibroblast activation (*33*) after bleomycin treatment (Fig. 1I). Exacerbated fibrosis in recipients of aged bone marrow was verified by histological scoring (Ashcroft score) and increased hydroxyproline levels in the lung tissue at D21 (peak fibrosis) (Fig. 1, J and K) and was already evident by D14 (fig. S2, A and B). Pulmonary transforming growth factor–β (TGF-β) levels (Fig. 1L) and fibrotic genes such as *Actb*, *Arg1*, *Vegf*, and *Col1a1* were elevated by D21 (Fig. 1M). To test whether hematopoietic aging promoted fibrosis by enhancing lung injury in the early inflammatory phase after bleomycin challenge (D7), we assessed the total protein concentration in the bronchoalveolar lavage fluid (BALF) (fig. S2C) and the number of apoptotic lung cells [terminal deoxynucleotidyl transferase–mediated deoxyuridine triphosphate nick end labeling (TUNEL)$^+$] but found no differences between the two recipient groups (fig. S2, D and E). Together, our data show that an aged bone marrow is sufficient to exacerbate the development of lung fibrosis, without altering the degree of bleomycin-induced lung injury.

An aged bone marrow autonomously promotes enhanced Mo-AM influx upon lung injury

Given the profibrotic role of bone marrow–derived Mo-AMs in the lungs (*15*), we assessed whether an aging bone marrow could affect Mo-AM accumulation upon bleomycin injury in mice. Although baseline levels remained similar (fig. S3A), young recipients of aged bone marrow had increased myeloid progenitors (GMPs) and mature myeloid cells (monocytes and neutrophils) in the bone marrow after bleomycin challenge (Fig. 2A and fig. S3, B and C). This was accompanied by elevated numbers of Mo-AMs, monocytes (Fig. 2B), neutrophils, and dendritic cells (fig. S3D) in the BALF post-bleomycin, mirroring naturally aged animals. Although most lung cell populations were efficiently reconstituted in both groups after transplantation (fig. S3, E and F), recipients of aged bone marrow had decreased numbers of TR-AMs (SiglecF^{hi} CD11b^{lo}) in the BALF and lung at baseline (Fig. 2C and fig. S3F).

To determine whether the increased Mo-AM influx in recipients of aged bone marrow resulted from enhanced availability of AM niche space, we shielded the thoraces of young recipient mice during irradiation and transplanted green fluorescent protein (GFP)$^+$ bone marrow cells from young or aged mice (Fig. 2D). There was minimal contribution of GFP$^+$ donor cells in the lungs before fibrosis induction (fig. S3G), and GFP$^+$ SiglecF^{lo} Mo-AMs infiltrated the lungs only once bleomycin was given (fig. S3H). Shielded mice that received aged bone marrow still experienced greater body weight loss during the course of bleomycin challenge (Fig. 2E). Despite bearing lung-tissue resident immune cells of young host origin (GFP$^-$) and displaying no deficit in the number of SiglecF^{hi} TR-AMs at baseline (Fig. 2, F and G), we observed an increased influx of GFP$^+$ Mo-AMs (Fig. 2, F and H) and neutrophils (fig. S3I) upon bleomycin challenge.

We then investigated whether young bone marrow could reduce Mo-AM influx in aged mice by transplanting young or aged bone marrow into irradiated aged mice (Fig. 2I). Despite the presence of aged lung tissue, young bone marrow protected aged mice from bleomycin-induced weight loss (Fig. 2J) and reduced Mo-AM (Fig. 2K), monocyte, and neutrophil (fig. S3J) numbers to levels comparable to those in young mice with young bone marrow at D7. Together, these data demonstrate that an aged bone marrow autonomously drives Mo-AM influx and is a key determinant of disease severity, irrespective of the age of the lung tissue or lung resident immune cells.

Mo-AMs from aged bone marrow display a delayed transition into a homeostatic phenotype

Once in the lungs, the phenotype acquired by Mo-AMs and the rate of transition into homeostatic macrophages in the tissue governs their functional outcome (*23*). We therefore analyzed macrophage dynamics from the initial inflammatory phase (D7) to the development of fibrosis (D14) using flow cytometry and transcriptomic analysis. D14 served as the fibrotic end point because two distinct

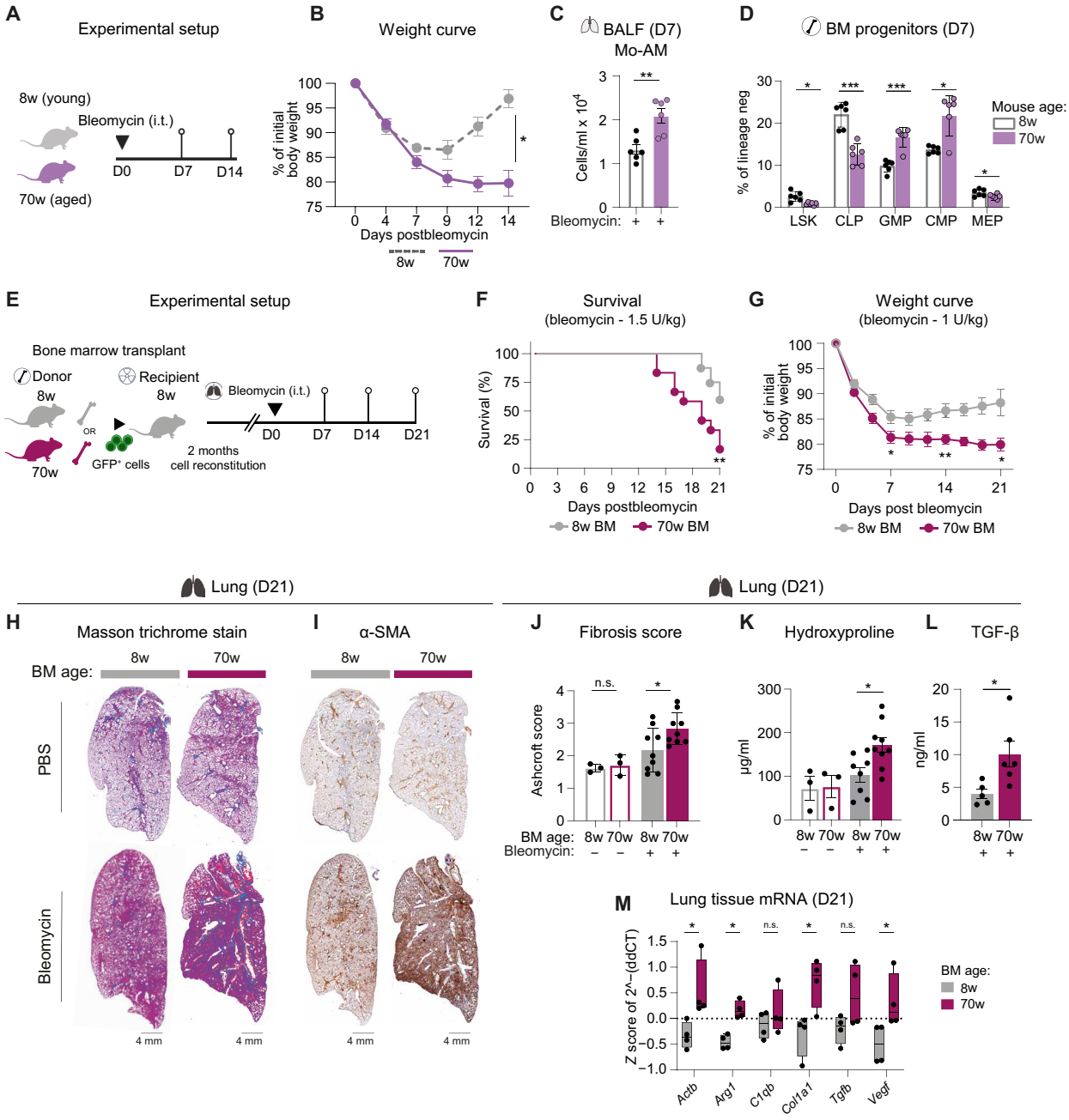

Fig. 1. An aged bone marrow exacerbates lung fibrosis. (**A**) Experimental setup. (**B** to **D**) Bleomycin (1 U/kg) was given to 8-week-old (8w) or 70-week-old (70w) C57BL/6J WT mice with end points taken seven (D7) or 14 days (D14) postchallenge ($n = 5$ to 7 per group per time point; i.t., intratracheal). (B) Body weight curve showing percentage loss of initial body weight after bleomycin challenge. (C) Absolute numbers of Mo-AMs from the BALF on D7 after bleomycin challenge. Mo-AMs gated as SiglecF^{lo} CD11b^{hi} from CD64^{+} MerTK^{+} cells. (D) Hematopoietic stem cell progenitors in the bone marrow expressed as percentage of lineage-negative cells (see fig. S1D; LSK, Sca1^{+} cKit^{+} cells; CMP, common myeloid progenitor; MEP, megakaryocyte-erythroid progenitor). (**E**) Experimental setup. (**F** to **M**) Young (8w) C57BL/6J WT recipient mice were lethally irradiated and transplanted with bone marrow cells from young (8w) or aged (70w) donor mice (GFP^{+} bone marrow cells). Two months postreconstitution, recipients were given bleomycin intratracheally ($n = 5$ to 10 per time point). (F) Survival curve until D21 postchallenge (1.5 U/kg, high bleomycin dose). (G) Body weight curve until D21 (1 U/kg, low bleomycin dose). [(H) and (I)] Histological sections of left lung lobe (D21) postbleomycin/PBS. (H) Masson trichrome staining for collagen deposition. (I) α-SMA staining for activated myofibroblasts. (J) Fibrosis quantified by a modified Ashcroft score of lung histology (D21). (K) Hydroxyproline quantification from lung tissue (D21). (L) ELISA of lung activated TGF-β (D21). (M) Gene expression analyzed by real-time quantitative PCR (qPCR) from lung homogenates. CT values relative to *Gapdh* (2^{-ddCT}), where ddCT stands for delta delta cycle threshold, shown as *z* score per gene across both groups ($n = 4$ per group). Data are representative of two or three independent experiments. Symbols on bar graphs represent individual mice. For (B), (G), (J), and (K), two-way ANOVA with Tukey's multiple comparison test was used; Student's two-tailed *t* test [(C) and (L)], multiple unpaired *t* tests with Welch correction followed by Holm-Šídák test (D), a log-rank (Mantel-Cox) test for survival curve (F), and multiple unpaired *t* tests (M) were used. Error bars represent SEM or SD. *$P \leq 0.05$; **$P < 0.01$; ***$P < 0.001$; n.s., not significant.

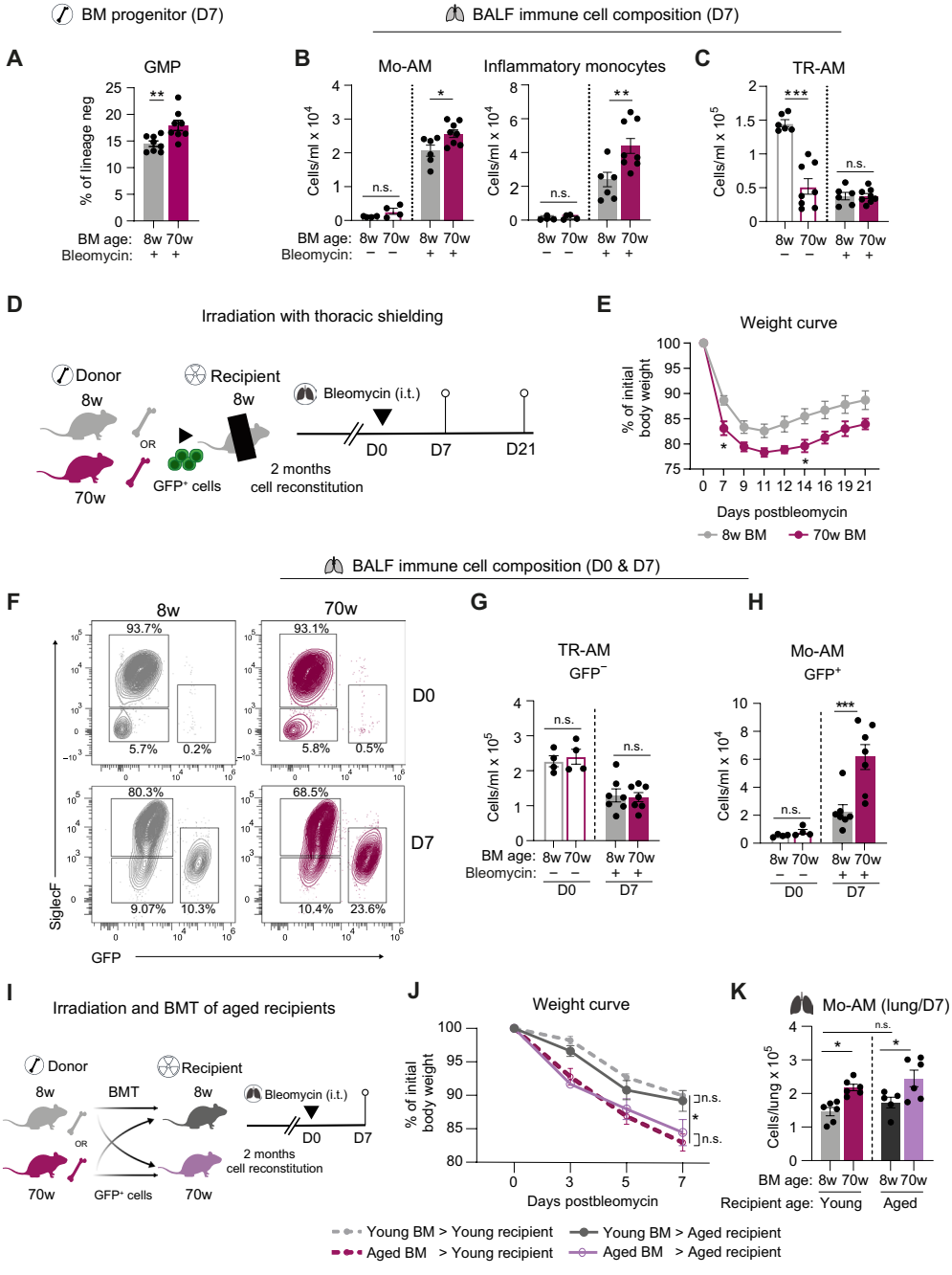

Fig. 2. An aged bone marrow autonomously promotes enhanced monocyte-derived alveolar macrophage influx upon lung injury. (**A** to **C**) Whole body irradiation (8w-old recipients) and bone marrow transplant with 8w or 70w donor cells, PBS/bleomycin (intratracheally) administered 2 months postreconstitution; parameters assessed at D7 ($n = 4$ to 9 per group). (A) GMPs from the bone marrow expressed as percentage of lineage-negative cells. (B) Absolute numbers of cells showing Mo-AMs (SiglecF^{lo} CD11b^{hi}) and inflammatory monocytes (Ly6C^{hi} CD11b^{+}) from the BALF. (C) Absolute numbers of TR-AMs (SiglecF^{hi} CD11b^{lo}) from BALF. (**D**) Experimental setup for [(E) to (H)] Young (8w) C57BL/6J WT recipient mice were irradiated with a lead shield placed over the thoracic cavity and transplanted with bone marrow cells from 8w or 70w donor mice (GFP^{+}); 2 months postreconstitution challenged with bleomycin ($n = 6$ to 8 per group with bleomycin; $n = 4$ per group at D0/baseline). (**E**) Body weight curve until D21. (**F**) Flow cytometry plots showing GFP^{+} and GFP$^{−}$ SiglecF^{hi} TR-AMs and SiglecF^{lo} MoAMs, respectively, in the BALF of 8w and 70w bone marrow recipients at D0 (baseline; top panel) and D7 (bottom panel). (**G**) Absolute numbers of TR-AMs (GFP$^{−}$ cells) and (**H**) Mo-AMs (GFP^{+} cells) from the BALF on D0 (baseline) and D7 (after bleomycin challenge). (**I**) Experimental setup for [(J) and (K)]. Young (8-week-old) and aged (70-week-old) C57BL/6J WT recipient mice were irradiated and transplanted with 8w or 70w GFP^{+} bone marrow cells 2 months postreconstitution, and recipients were administered bleomycin (intratracheally) ($n = 5$ to 7 per group). (**K**) Body weight curve until D7. (**L**) Absolute numbers of Mo-AMs from whole lung tissue at D7. Data are representative of three independent experiments [(A) to (C)] or two independent experiments [(D) to (L)]. Symbols on bar graphs represent individual mice. Flow cytometry plots and histological sections are representative of each group. (A) Student's two-tailed *t* test, [(B), (C), and (G) to (H)] two-way ANOVA with post hoc Šídák's multiple comparisons test, and [(E), (J), and (K) two-way ANOVA with Tukey's post hoc multiple comparisons test were used [mixed effect for (E)]. Error bars represent SEM. $*P \leq 0.05$; $**P < 0.01$; $***P < 0.001$; n.s., not significant.

macrophage populations can still be distinguished on the basis of SiglecF expression at this time (Fig. 3A). In both groups, there was an initial depletion of SiglecF^{hi} TR-AMs and influx of SiglecF^{lo} Mo-AMs on D7 after bleomycin (Fig. 3B). However, recipients of aged bone marrow showed slower SiglecF^{hi} TR-AM restoration and prolonged accumulation of SiglecF^{lo} Mo-AMs in the lung tissue (Fig. 3, B and C). Mo-AMs initially express low levels of SiglecF and gradually up-regulate SiglecF as they become increasingly tissue-resident–like (*34*). Although Mo-AMs from both young and aged bone marrow displayed comparably low SiglecF expression at

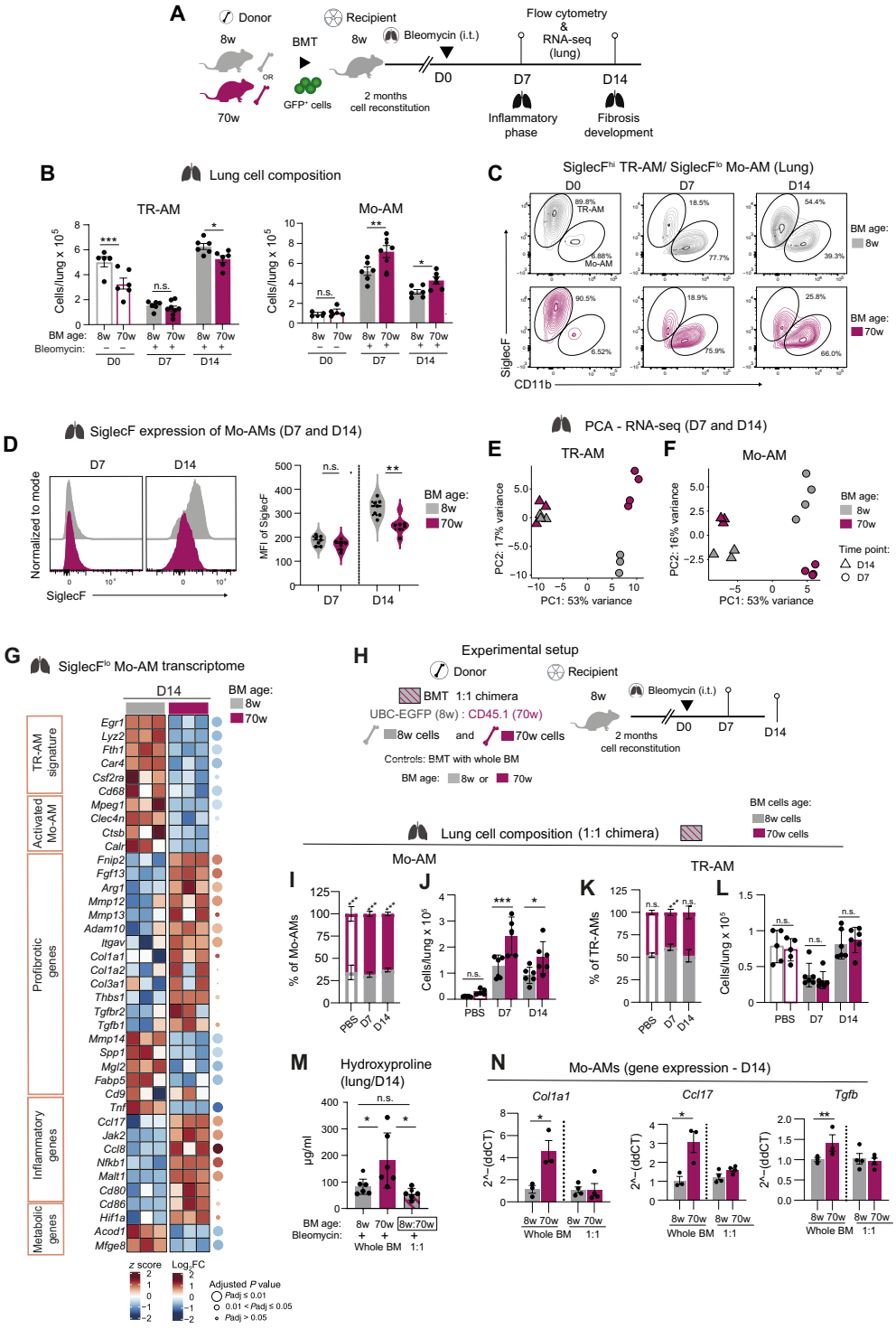

Fig. 3. Mo-AMs from aged bone marrow display a delayed transition into a homeostatic phenotype. (**A**) Experimental setup. (**B** to **G**) Lung TR-AMs and Mo-AMs from recipients of 8w or 70w bone marrow analyzed by flow cytometry and bulk RNA-seq (sorted cells) at D7 (inflammatory phase) and D14 (fibrosis development) postbleomycin. (B) Absolute cell numbers of lung TR-AMs and Mo-AMs. (C) Representative flow cytometry plots at D0, D7, and D14. (D) SiglecF expression on Mo-AMs at D7 and D14. Right: Quantification of mean fluorescence intensity [MFI; arbitrary units (a.u.)]. (**E** and **F**) PCA of sorted lung (E) TR-AMs and (F) Mo-AMs from recipients of 8w and 70w bone marrow [D7 and D14 ($n = 4$/D7 and $n = 3$/D14)]. (**G**) Heatmap of selected differentially expressed genes (DEGs) expressed by Mo-AMs (D14, $n = 3$ per group) (*15*, *16*, *37*, *38*). Heatmap color: *z* score of normalized log(CPM) across both groups per gene; columns: individual samples; circle sizes: adjusted *P* value; circle colors: $\log_2$ fold change (FC) of 70w versus 8w bone marrow recipient Mo-AMs. Extended gene list in data file S4. (**H**) Experimental setup for (**I** to **N**). 8w recipient mice irradiated and transplanted with bone marrow cells from young (8w, GFP$^+$ bone marrow) and aged (70w, CD45.1 bone marrow) donor mice in a 1:1 ratio. PBS or D7 and D14 postbleomycin (I) percentage of lung Mo-AMs within the total Mo-AM population and (J) absolute cell numbers of lung Mo-AMs from 8w (GFP$^+$) or 70w (CD45.1$^+$) cells. (K) Percentage of lung SiglecF^{hi} TR-AMs within the total TR-AM population and (L) absolute cell counts of lung SiglecF^{hi} TR-AMs from 8w (GFP$^+$) or 70w (CD45.1$^+$) cells. (M) Hydroxyproline quantification (lung tissue) of recipients reconstituted with 8w (gray bar), 70w bone marrow cells (purple bar) and (8w): 70w bone marrow chimera (1:1; gray and purple-striped bar) at D14 postbleomycin. (N) Gene expression (real-time qPCR) from lung Mo-AMs sorted from recipients of 8w or 70w whole bone marrow transplant (left panel) and 8w (GFP$^+$) and 70w (CD45.1$^+$) 1:1 chimeric recipient (right panel) at D14 postbleomycin. Data are representative of three independent experiments (flow cytometry), $n = 5$ to 8 per group per time point [(B) to (D)] and $n = 5$ or 6 per time point of one independent experiment [(H) to (N)]. [(B), (D), and (I) to (L)] Two-way ANOVA with Tukey's post hoc multiple comparisons test, (M) one-way ANOVA, and (N) two-way ANOVA with post hoc Šídák's multiple comparisons test were used. Error bars represent SD.*$P \leq 0.05$; **$P < 0.01$; ***$P < 0.001$; n.s., not significant.

D7, aged Mo-AMs failed to up-regulate SiglecF at D14 (Fig. 3D), indicating delayed maturation. Using the thorax-shielded bone marrow chimera model (from Fig. 2D) to trace the transition of donor bone marrow–derived GFP$^+$ SiglecF^{lo} Mo-AMs into SiglecF^{hi} TR-AMs over time, we found that no GFP$^+$ macrophages expressed high SiglecF levels at D7 in both groups and that most GFP$^+$ Mo-AMs transitioned to a SiglecF^{hi} TR-AM state by D21 and D42 (fig. S4A). However, the percentage of GFP$^+$ Mo-AMs that coexpressed SiglecF from an aged bone marrow remained lower when compared with young bone marrow–derived cells, further highlighting delayed acquisition of a TR-AM phenotype (fig. S4, A and B).

We next analyzed the transcriptome of Mo-AMs and TR-AMs at D7 and D14 after bleomycin challenge (Fig. 3A). Principal components analysis (PCA) revealed that the TR-AM population became increasingly similar over time between the two groups (Fig. 3E) and showed signs of reconstitution by monocyte-derived cells by D14 [increased expression of *Ccr2*, *Ccr5*, *colony stimulating factor 1 receptor* (*Csf1r*), and *histocompatibility 2, class II antigen A, beta 1* (*H2-Ab1*)] (fig. S4C and data file S1). However, considerable differences persisted between young and aged bone marrow–derived Mo-AMs at D14 (Fig. 3F), with distinctive gene expression patterns across this transitional phase between the two groups (fig. S4D and data file S2). At D7 postbleomycin, Mo-AMs from aged bone marrow exhibited an early profibrotic profile [elevated expression of *secreted phosphoprotein 1* (*Spp1*), *collagen type I alpha 2* (*Col1a2*), *Col3a1*, and *tissue inhibitor of metalloproteinase 3* (*Timp3*)], although inflammatory gene expression (*Il1b*, *Nfkb1*, and *Cxcl2*) was lower compared with Mo-AMs from young bone marrow (fig. S4E and data file S3). Whereas aged Mo-AMs up-regulated *lymphocyte antigen 6 family member C1* (*Ly-6c1*), *Ly-6a*, and *Cd34*, a signature of their early monocytic legacy, expression of monocyte-to-macrophage differentiation markers (*Lgals3*, *Foxp1*, and *Csf2rb*) was reduced (fig. S4E) (*35*, *36*). In contrast, at D14, aged Mo-AMs displayed delayed but heightened expression of key pro-inflammatory mediators (*Nfkb1*, *Malt1*, and *Jak2*), chemokines (*Ccl17* and *Ccl8*), and activation markers (*Cd80* and *Cd86*), whereas young Mo-AMs already down-regulated most inflammatory genes (Fig. 3G and data file S4). Aged Mo-AMs maintained a more pronounced profibrotic signature of collagenases (*Col1a1* and *Col1a2*), matrix metalloproteases (*Mmp12* and *Mmp13*), *folliculin interacting protein 2* (*Fnip2*), *fibroblast growth factor 13* (*Fgf13*), and *transforming growth factor beta 1* (*Tgfb1*), with young Mo-AMs expressing only a specific subset of profibrotic genes (*Mmp14*, *Spp1*, and *Fabp5*). By D14, young Mo-AMs had up-regulated homeostatic TR-AM genes, including *Car4*, *Fth1*, *Lyz2*, and *CD68* (*37*) along with metabolic regulators such as *Acod1* and *Mfge8*, known to mitigate the fibrotic response (*38*, *39*). In contrast, Mo-AMs from recipients of aged bone marrow failed to do so (Fig. 3G). Together, these data show that Mo-AMs derived from an aged bone marrow experience a delayed transition toward a tissue-resident phenotype, coinciding with the slower return to homeostasis after lung injury.

Cell-intrinsic factors determine Mo-AM influx, whereas environmental signals delay their transition with age

To investigate the extent of cell-intrinsic and cell-extrinsic factors influencing Mo-AM phenotype, we exposed young and aged Mo-AMs/TR-AMs to identical lung microenvironments. Irradiated young recipient mice (CD45.2 background) were reconstituted with a 1:1 mix of young (GFP$^+$) and aged (CD45.1) donor bone marrow cells (Fig. 3H). Posttransplant, young and aged bone marrow cells repopulated the bone marrow and lungs with a similar efficiency overall (fig. S5A). However, repopulation by aged CD45.1$^+$ bone marrow–derived cells was characterized by a strong skewing toward increased myeloid cells and decreased lymphoid cells in the bone marrow and lung at baseline [phosphate-buffered saline (PBS)–treated mice] (fig. S5, B to E). This skewed distribution persisted after bleomycin challenge (fig. S5, F to I). The ratio of aged Mo-AMs [and interstitial macrophages (IMs) in the PBS control mice/baseline] was higher at D7 and D14 postbleomycin (Fig. 3, I and J, and fig. S5J), indicating that the increased recruitment of aged Mo-AMs is due to an intrinsic myeloid bias in aged bone marrow or an increased cell-intrinsic proliferative capacity of aged monocytes/Mo-AMs. Conversely, PBS-treated mice had a similar reconstitution of young and aged bone marrow–derived TR-AMs in the lungs (Fig. 3, K and L, and fig. S5K), unlike the baseline TR-AM deficit observed after transplantation of aged bone marrow alone (Fig. 2C), with no difference in the absolute cell counts of TR-AMs at D7 and D14 postbleomycin (Fig. 3L). Together, these findings suggest that, whereas cell-intrinsic factors determine absolute Mo-AM numbers, the presence of young hematopoietic cells may be sufficient to maintain TR-AM numbers or drive efficient Mo-AM–to–TR-AM transition.

Lung hydroxyproline content (Fig. 3M) and collagen deposition in the lungs at D14 postbleomycin was reduced in 1:1 mixed chimeric mice when compared with mice transplanted with aged cells alone (fig. S5, L and M), suggesting that young hematopoietic cells mitigate exacerbated fibrosis in spite of increased influx of aged Mo-AMs. We thus speculated that fibrosis severity was not solely driven by initial Mo-AM numbers but further determined by the immune microenvironment that shapes Mo-AM transcriptional states and transition. Although Mo-AMs sorted from mice that received only aged bone marrow had up-regulated key fibrotic and inflammatory genes (*Col1a1*, *Ccl17*, and *Tgfb*) in comparison with young Mo-AMs, young and aged Mo-AMs isolated from 1:1 chimeric mice did not display these differences (Fig. 3N). These findings indicate that the increased number of Mo-AMs is autonomously driven by an aged bone marrow and cell-intrinsic differences in aged monocytes/Mo-AMs. In contrast, the transcriptional phenotype acquired by Mo-AMs in the lungs, as well as their profibrotic features, seems to be regulated by extrinsic environmental factors derived from other hematopoietic cells.

Hematopoietic aging decreases IL-10 availability and drives a pro-inflammatory milieu in the lung

Given the delayed transition of aged Mo-AMs to a homeostatic TR-AM phenotype, we examined lung microenvironmental signals that might influence this process. By D7 postbleomycin, mice reconstituted with aged bone marrow displayed an altered lung cytokine profile, with increased pro-inflammatory mediators such as interferon-γ (IFN-γ), IL-6, CXCL1, and CCL17 but reduced IL-10 and IL-13 levels (Fig. 4A and fig. S6A) with a corresponding transcriptional state in lung tissue (fig. S6B). The most notable difference between the groups after bleomycin-induced injury was the substantially lower IL-10 levels, which persisted through the inflammatory and fibrotic phases (Fig. 4B). Because IL-10 is a key anti-inflammatory cytokine (*40*), we hypothesized that reduced IL-10 availability could impair timely resolution of bleomycin-induced lung injury. To test this, we treated young adult mice with a neutralizing IL-10 antibody intranasally between D0 and D7 (Fig. 4C). IL-10 neutralization

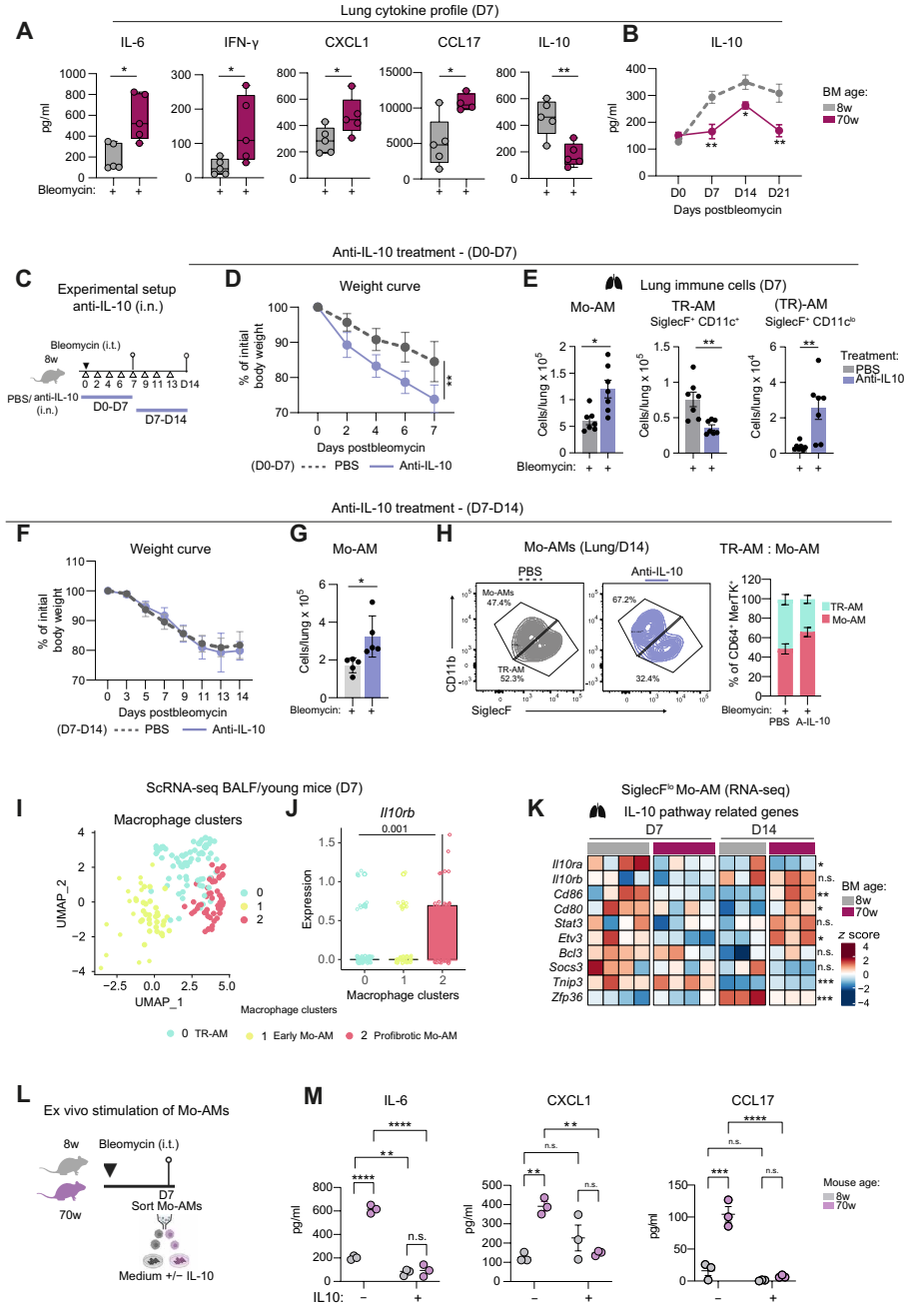

Fig. 4. Hematopoietic aging decreases IL-10 availability and drives a pro-inflammatory milieu in the lung. (**A**) Cytokine analysis of lung homogenates from recipients of 8w and 70w bone marrow at D7 postbleomycin. (**B**) ELISA of IL-10 from lung homogenate at D0, D7, D14, and D21 postbleomycin. (**C**) Experimental setup for (**D** to **I**) 8-week-old C57BL/6J mice given bleomycin (intratracheally) and intranasally (i.n.) treated with anti–IL-10 antibody or PBS at the indicated time points (D0 to D7) or (D7 to D14) until an end point of D7 or D14. (D) Weight curve until D7. (E) Absolute numbers of lung myeloid cells [Mo-AMs, TR-AMs (SiglecF^{hi} CD11b^{lo} CD11c^{hi}), and (TR)-AM–like cells (SiglecF^{hi} CD11b^{lo} CD11c^{lo})]. (F) Weight curve until D14. (G) Absolute numbers of lung Mo-AMs at D14. (H) Representative flow cytometry plots and bar graphs showing percentage of TR-AMs and Mo-AMs expressed as percentage of MerTK^{+} CD64^{+} cells. (I) Seurat clustering of three macrophage populations identified from scRNA-seq from the BALF of 8-week-old mice at D7 postbleomycin (cluster gene list in data file S5). (**J**) Expression of *Il10rb* on clusters 0 (TR-AMs), 1 (early Mo-AMs), and 2 (profibrotic Mo-AMs). (**K**) Heatmaps of transcriptomic analysis of selected IL-10–related genes on sorted lung Mo-AMs from recipients of 8w and 70w bone marrow at D7 and D14 postbleomycin ($n = 3$ or 4 per group). Heatmap color represents z score of log(CPM) normalized expression across all four groups (8w/D7; 70w/D7; 8w/D14; 70w/D14) per gene. Columns represent individual samples (gene expression data in data files S3 and S4 for D7 and D14, respectively). (**L**) Experimental setup. (**M**) Mo-AMs were sorted from 8w- or 70w-old WT mice at D7 after bleomycin and cultured ex vivo for 24 hours in medium with or without IL-10 ($n = 4$ per group, cells sorted and pooled together in three technical replicates per group). (M) Cytokine secretion analysis 24 hours postculture/stimulation (absolute values in pg/ml). For (F) and (G), BALF cells from six mice were pooled and sequenced. [(A), (E), (G), and (H)] Student's two-tailed unpaired t test, (B) multiple unpaired t test, [(D), (F), (K), and (M)] a two-way ANOVA with Bonferroni and Tukey's post hoc multiple comparisons test [overall column factor for (K); individual comparisons in data file S10], and (J) a Wilcoxon rank sum test with Bonferroni correction (Seurat) were used. Error bars represent SEM or SD. *$P \leq 0.05$; **$P < 0.01$; ***$P < 0.001$; ****$P < 0.0001$; n.s., not significant.

strongly increased weight loss (Fig. 4D) and reduced predicted survival post-D7 (fig. S6C). By D7, anti-IL-10–treated mice showed increased Mo-AM numbers, reduced TR-AMs, and the emergence of a CD11c^{low} CD11b^{hi} SiglecF+ (TR)-AM population (Fig. 4E and fig. S6D), suggesting that IL-10 maintains homeostatic TR-AMs. To assess whether IL-10 had an impact on Mo-AM maturation, we neutralized IL-10 in the lungs from D7 to D14 after bleomycin challenge (Fig. 4C). Although body weight loss was unaffected (Fig. 4F), IL-10 neutralization increased Mo-AM accumulation by D14 (Fig. 4, G and H), with a decreased resolutory (CD206$^+$) (*41*) and increased activated (CD86$^+$) (*42*) Mo-AM phenotype (fig. S6E), indicating that IL-10 is necessary for efficient Mo-AM transition into a homeostatic state.

We next asked whether Mo-AM differentiation or activation was influenced by IL-10 in the lung microenvironment. Single-cell RNA sequencing (scRNA-seq) of immune cells from the BALF of young adult mice identified three populations of macrophages in the alveolar space during the inflammatory phase (D7) after bleomycin challenge: TR-AMs [cluster 0, *lysozyme 2* (*Lyz2*), *Ccl6*, and *ferritin light polypeptide 1* (*Ftl1*) expression], cells of recent monocyte origin or early Mo-AMs (cluster 1, high *Ccr2*, *CD74*, and *H2-A* expression), and profibrotic Mo-AMs [cluster 2 with high expression of *MAF basic leucine zipper transcription factor B* (*Mafb*), *matrix metallopeptidase 14* (*Mmp14*), *integrin alpha M* (*Itgam*), and *Cd36*] (Fig. 4I and fig. S6, F and G). Only cluster 2 profibrotic Mo-AMs expressed elevated levels of *Il10rb*, encoding the IL-10 receptor (Fig. 4J and data file S5). Further transcriptomic analysis of Mo-AMs revealed that IL-10 signaling downstream targets, including *Tnip3*, *Etv3*, *Cd80*, *Cd86*, and *Stat3* (*43*, *44*), were induced in young Mo-AMs at D7 and promptly down-regulated by D14, whereas aged Mo-AMs showed a deferred expression of these genes by D14 (Fig. 4K).

To assess the direct effects of IL-10 on the Mo-AM phenotype, we sorted Mo-AMs from young or aged mice on D7 postbleomycin and stimulated them ex vivo with IL-10 (Fig. 4L). At baseline (without stimulation), aged Mo-AMs showed increased IL-6, CXCL1, and CCL17 cytokine secretion and gene expression levels compared with young Mo-AMs (Fig. 4M and fig. S6, H and I). IL-10 stimulation efficiently suppressed this inflammatory signature in both groups (Fig. 4M and fig. S6, H and I), demonstrating comparable responsiveness to IL-10. Conversely, granulocyte-macrophage colony-stimulating factor (GM-CSF), essential for TR-AM maintenance (*39*), had no impact on the inflammatory profile (fig. S6J). These data highlight the importance of environmental IL-10 in determining the Mo-AM response at this early juncture and that suppressed IL-10 levels, such as during hematopoietic aging, sustains their inflammatory phenotype.

Hematopoietic aging restricts lung IL-10–producing T_{regs} upon lung injury

To identify cellular sources of IL-10 in the lung environment affected by hematopoietic aging, we analyzed intracellular IL-10 in major lung immune cells postbleomycin. Bone marrow age did not affect IL-10 levels in IL-10–producing innate immune cells, including neutrophils, TR-AMs, Mo-AMs, IMs, innate lymphoid cells (ILCs), and natural killer (NK) cells (fig. S7A) (*45*). However, CD4$^+$ T cells in young mice engrafted with aged bone marrow produced less IL-10 upon bleomycin challenge (Fig. 5A). Specifically, CD25$^+$ cells and CD4$^+$ CD25$^+$ Foxp3$^+$ T_{regs} had lower IL-10 levels (Fig. 5B and fig. S7B). Although the total number of CD4$^+$ T cells after bleomycin challenge was similar (fig. S7C), IL-10$^+$ CD4$^+$ T cell abundance was lower in recipients of aged bone marrow (Fig. 5C; gating strategy in fig. S7D) with a reduced frequency of Foxp3$^+$ T_{regs} among IL-10$^+$ immune cells (fig. S7E). Although T_{regs} expanded upon bleomycin injury in both groups, an aged bone marrow curtailed T_{reg} expansion (Fig. 5, D and E) at both the inflammatory (D7) and fibrotic (D14) phases, with pronounced reductions of the IL-10$^+$ subset (Fig. 5F). In contrast, CD49b$^+$ Lag3$^+$ type 1 regulatory T (Tr1) cells, other known IL-10 producers (*46*), were unaffected by bone marrow age (fig. S7F). The diminished T_{reg} expansion was associated with increased T helper 1 (T_H1) (T-bet$^+$) and reduced T_H17 [retinoic acid receptor–related orphan receptor gamma t (RORγt)$^+$] numbers (fig. S7G).

Although T_{regs} can be radioresistant (*47*), young host-derived T_{regs} in the lungs were minimal (fig. S7H), and all IL-10$^+$ Foxp3$^+$ were donor derived (fig. S7I). A reduction in IL-10$^+$ T_{regs} was also recapitulated in naturally aged mice postbleomycin (fig. S7, J and K). Using the thoracic shielding model to distinguish between tissue-resident (GFP$^-$) and peripheral (GFP$^+$) T_{regs}, we found a specific reduction in lung GFP$^+$ Foxp3$^+$ and GFP$^+$ IL-10$^+$ T_{regs} (Fig. 5G) and IL-10 levels (fig. S7L) in mice engrafted with aged bone marrow. Collectively, our results show that reduced IL-10 in the lungs of naturally aged mice and recipients of aged bone marrow display impaired recruitment of IL-10$^+$ T_{regs} after bleomycin challenge.

Transcriptomic analysis of CD25$^+$ CD4$^+$ T cells on D7 postbleomycin revealed substantial differences in the expression of key T_{reg} markers (*48*), including *Ctla-4*, *Icos*, and *Tnfrsf18I* (Fig. 5H and data file S6). In mice that received aged bone marrow, there was a notable reduction in the absolute numbers of inducible costimulator (ICOS)$^+$ and glucocorticoid-induced tumor necrosis factor receptor family related protein (GITR)$^+$ T_{regs} (fig. S8A) and a shift toward T_H1-like T_{regs} (T-bet$^+$), whereas no differences were detected in T_H17-like (Rorγt$^+$) or T_H2-like T_{regs} (Gata3$^+$) (fig. S8, B and C), indicating that hematopoietic aging leads to both numerical and transcriptional alterations in lung T_{regs}.

To contextualize these findings, we integrated data from the Human Lung Cell Atlas (HLCA) (*49*), comparing transcriptional profiles from young and aged healthy individuals, patients with IPF, and young and aged patients with COVID-19. We used COVID-19 samples to compare young and aged individuals after acute lung injury, given that IPF data are predominantly derived from aged patients with end-stage disease (fig. S8D and data file S7). T_{regs} (fig. S8E) from healthy aged individuals showed increased expression of *IFNG*, indicating a T_H1-like shift similar to our observations in mice, whereas the levels of *cytotoxic T-lymphocyte-associated protein 4* (*CTLA4*), *forkhead box P3* (*FOXP3*), and *interleukin 2 receptor alpha chain* (*IL2RA*) tended to be lower (Fig. 5I and data fileS8). Aged T_{regs} were also enriched for inflammation- and fibrosis-associated genes at baseline (Fig. 5J and data file S8). Mo-AMs from patients with IPF expressed canonical profibrotic genes (*SPP1*, *COL6A*, and *FN1*) (fig. S8F and data file S9) (*32*, *49*, *50*). Similarly, aged COVID-19 Mo-AMs exhibited an activated, profibrotic phenotype with elevated *ficolin 1* (*FCN1*), *CXCL8*, *CCL4*, and *platelet derived growth factor subunit A* (*PDGFA*) expression (fig. S8F) (*51*). Together, these data show that hematopoietic aging hampers the T_{reg} response, reducing T_{reg}-derived IL-10 in mice, with age-related T_{reg} alterations also observed in aged human lung samples.

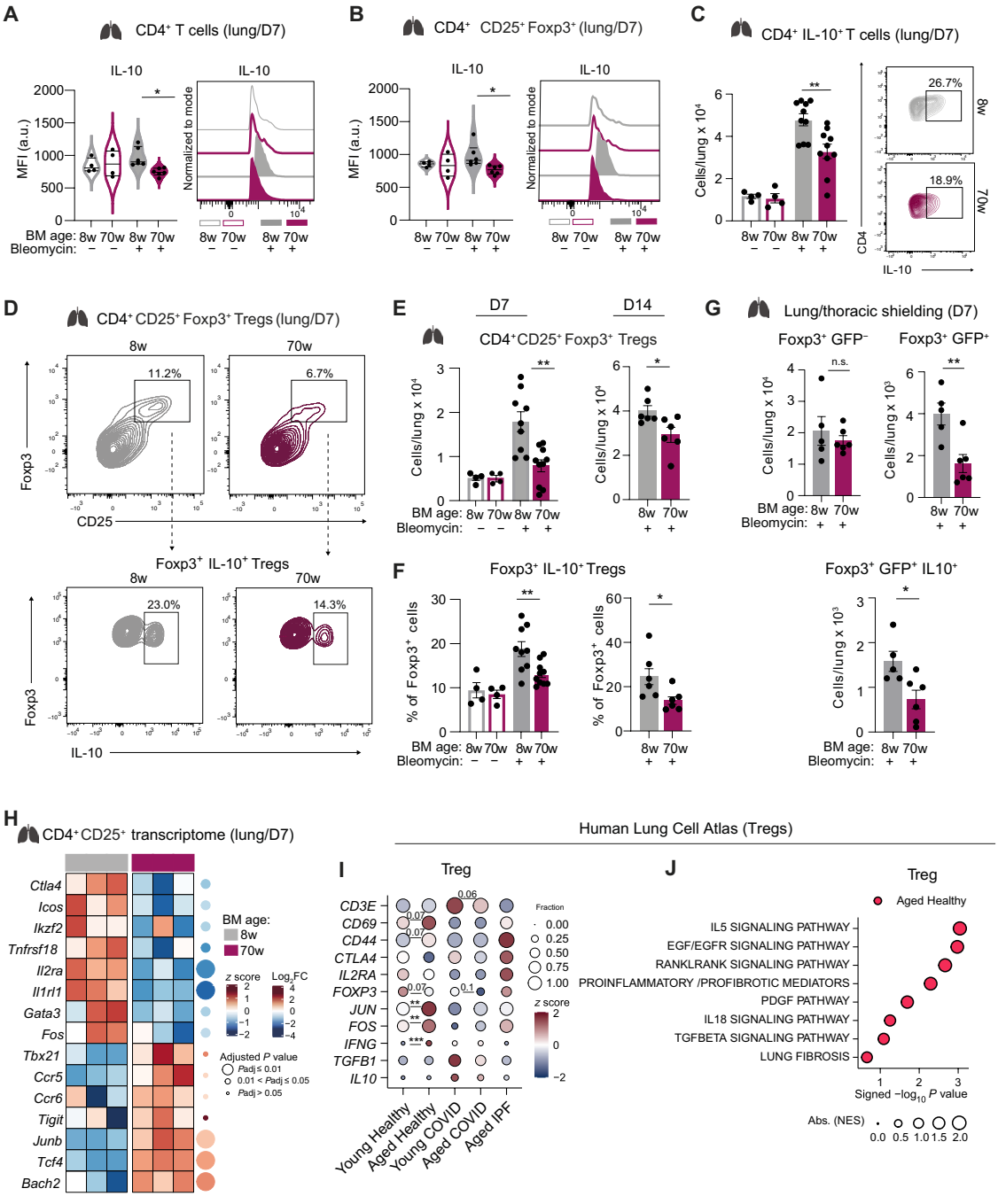

Fig. 5. Hematopoietic aging restricts lung IL-10$^+$ T_{regs} upon lung injury. (**A**) Histograms of intracellular IL-10 staining and MFI quantification of IL-10 by flow cytometry of lung CD4$^+$ T cells from recipients of (8w) or (70w) bone marrow at D7 (PBS/bleomycin treatment). (**B**) Histograms of intracellular IL-10 staining of lung CD4$^+$ CD25$^+$ Foxp3$^+$ cells and MFI quantification of IL-10. (**C**) Absolute cell numbers of lung CD4$^+$ IL-10$^+$ T cells, representative flow cytometry plots of percentage of lung IL-10$^+$ CD4$^+$ T cells from recipients of (8w) and (70w) bone marrow at D7 postbleomycin. (**D**) Representative flow cytometry plots of (top panel) lung CD4$^+$ CD25$^+$ Foxp3$^+$ cells and (bottom panel) Foxp3$^+$ IL-10$^+$ cells D7 postbleomycin. (**E**) Absolute cell numbers of lung CD4$^+$ CD25$^+$ Foxp3$^+$ cells and (**F**) percentage of Foxp3$^+$ cells expressing intracellular IL-10 of PBS-treated, D7 and D14 postbleomycin (n = 4 to 10). (**G**) Absolute numbers of lung CD4$^+$ Foxp3$^+$ GFP$^-$ or GFP$^+$ and Foxp3$^+$ GFP$^+$ IL-10$^+$ cells from recipients of irradiation with thoracic shielding at D7 postbleomycin (n = 5 or 6). (**H**) Transcriptomic analysis of CD4$^+$ CD25$^+$ lung cells sorted at D7 postbleomycin from the lungs of recipients of 8w or 70w bone marrow. Heatmap depicting selection of DEGs (n = 3 per group). (**I**) Transcriptomic analysis of T_{regs} from the Human Lung Cell Atlas. Heatmap showing selection of gene expression with a z score per gene across all groups: young healthy, aged healthy, young COVID, aged COVID, and aged IPF (see Materials and Methods). (**J**) Gene set enrichment analysis showing selected significantly enriched pathways in T_{regs} from aged healthy samples. Data are representative of three independent experiments [(A) to (F)] or two independent experiments (G). Symbols on bar graphs represent individual mice. [(A), (B), (C), (E) (D7), and (F) (D7)] Two-way ANOVA with Tukey's post hoc multiple comparison and [(E) (D14), (F) (D14), and (G)] Student's two-tailed unpaired t test were used. For (H), (I), and (J), differential expression analysis (DEA) by Limma was used (data file S8). Error bars represent SEM. *$P \leq 0.05$; **$P < 0.01$; ***$P < 0.001$; n.s., not significant.

IL-10–producing T_{regs} promote Mo-AM maturation and attenuate fibrosis

To examine whether T cell–derived IL-10 affects Mo-AM responses and fibrosis development, we generated 1:1 mixed bone marrow chimeras using T cell receptor α knockouts (TCR-$\alpha^{-/-}$) and IL-$10^{-/-}$ bone marrow (fig. S9A), which lack IL-10–producing T cells but retain functional B and myeloid compartments. Controls included wild-type (WT) (8-week-old:8-week-old or 70-week-old:70-week-old) TCR-$\alpha^{-/-}$:WT (8-week-old), or IL-$10^{-/-}$:WT (8-week-old) chimeras (fig. S9A). TCR-$\alpha^{-/-}$:IL-$10^{-/-}$ chimeras exhibited increased disease severity postbleomycin compared with controls (fig. S9, B and C) and reduced IL-10 levels, confirming T cells as a major IL-10 source in the lungs (fig. S9D). Although Mo-AM numbers were comparable to WT controls at D7 (fig. S9E), they remained elevated by D14 (fig. S9F), indicating persistent Mo-AM accumulation in the absence of T cell–derived IL-10.

Transcriptomic and cellular interaction analysis among IL-10–expressing cell types (TR-AMs, Mo-AMs, monocytes, $CD4^+CD25^-$, and $CD4^+CD25^+$ cells) suggested that $CD25^+$ T cells were the primary IL-10 source interacting with IL-10R–expressing monocytes and Mo-AMs in young bone marrow recipients (Fig. 6A). This interaction was reduced in recipients of aged bone marrow (Fig. 6B and fig. S9G). Moreover, intravenous labeling of $CD45^+$ cells at D7 after bleomycin challenge revealed that T_{regs}, like Mo-AMs, localized to the lung parenchyma (fig. S9, H and I), and immunohistology demonstrated that $Foxp3^+$ cells were in close proximity to $F4/80^+$ macrophages in bleomycin-challenged lungs (fig. S9J).

We therefore asked how the reduction of these $CD25^+$ T cells observed upon hematopoietic aging affected the disease course and Mo-AM response. Partial depletion of $CD25^+$ cells including T_{regs}, with an anti-CD25 antibody, during the inflammatory phase postbleomycin [D(−2) to D7] (fig. S10, A and B) caused weight loss (fig. S10C) and decreased lung IL-10 levels (fig. S10D) but had no impact on Mo-AM numbers at D7 (fig. S10E). In contrast, depletion during the fibrotic phase (D7 to D14) (fig. S10F) did not affect body weight (fig. S10G) but increased Mo-AM accumulation by D14 (fig. S10, H to J). To model the age-related reduction in T_{regs} observed throughout the disease course (Fig. 5E), we used depletion of regulatory T cells (DEREG) Foxp3–enhanced green fluorescent protein reporter mice and partially depleted T_{regs} via intratracheal diphtheria toxin (DT) administration between D(−2) and D14 (Fig. 6C and fig. S10K). Both IL-10^+ and IL-10^- T_{reg} numbers were reduced, and this was further associated with an expansion of T-bet^+ T helper cells during fibrosis (fig. S10L), thus resembling key features we had observed upon hematopoietic aging. T_{reg} reduction led to a pronounced decrease in body weight (Fig. 6D), increased collagen deposition, higher Ashcroft score (Fig. 6, E and F), lower lung IL-10 levels, and elevated inflammatory cytokines (Fig. 6G and fig. S10M) as compared with control mice. DEREG mice had elevated numbers of Mo-AMs at D14 with lower SiglecF expression levels (Fig. 6, H to J), indicating delayed Mo-AM maturation.

To verify whether T_{reg} depletion specifically during the fibrotic development phase affected Mo-AM transition, we treated Foxp3-DTR mice (*52*), a model that allowed us to efficiently ablate T_{regs} over a shorter period of time, with DT administered only from D7 to D14 postbleomycin (Fig. 6K and fig. S10, N and O). This resulted in increased weight loss (fig. S10P), elevated lung hydroxyproline levels (fig. S10Q), Mo-AM accumulation with lower SiglecF expression (Fig. 6, L to N), a reduction in resolutory-like ($CD206^+$) Mo-AMs, and an increase in activated Mo-AMs ($CD86^+$) (fig. S10R) compared with control mice. This was confirmed in a bone marrow transplant model using Foxp3–DT receptor (DTR) or Rosa26iDTR donors to compare DT treatment during the full course (D0 to D14) versus the fibrotic phase (D7 to D14) after bleomycin challenge (fig. S10, S and T). Mice lacking T_{regs} exhibited weight loss and increased Mo-AM accumulation, whereas DT treatment alone caused no adverse effects in PBS-treated controls (D0 to D14) (fig. S10, U and V).

Last, to determine whether Foxp3-T_{reg}-derived IL-10 specifically reduces Mo-AM accumulation, independent of other T_{reg} mechanisms, we generated 1:1 mixed bone marrow chimeras using Foxp3-DTR and IL-$10^{-/-}$ donors. This setup allowed assessment of T_{reg}-derived IL-10's role in Mo-AM transition without fully depleting T_{regs} (Fig. 6O). Control groups were transplanted with a 1:1 ratio of Foxp3-DTR: Foxp3-DTR; Foxp3-DTR: 8-week-old WT; or Foxp3-DTR: 70-week-old WT bone marrow. Postreconstitution, all groups received DT treatment (D0 to D14). Mixed chimeras of Foxp3-DTR with either aged bone marrow or IL-$10^{-/-}$ bone marrow exhibited pronounced weight loss, similar to mice completely lacking T_{regs} (reconstituted only with Foxp3-DTR) (Fig. 6P) and had elevated lung hydroxyproline levels (fig. S11A) when compared with mice that received young bone marrow. Mice deficient in IL-10–producing T_{regs} had increased numbers of lung Mo-AMs at D14 (Fig. 6Q) that had low SiglecF expression (Fig. 6R), akin to those devoid of T_{regs}. This indicates that the absence of IL-10 from T_{regs}, even without a notable reduction in T_{reg} numbers (fig. S11B), is sufficient to cause Mo-AM accumulation, supporting the critical role of T_{reg}-derived IL-10 as a mediator that facilitates the efficient maturation of Mo-AMs. This parity between the depletion of IL-10–producing T_{regs} and their reduction due to hematopoietic aging underscores their essential regulatory role in shaping Mo-AM transition and lung fibrosis outcome after bleomycin challenge.

DISCUSSION

Tissue injury triggers a cascade of inflammatory events, recruiting and activating immune and nonimmune cells to coordinate repair (*4*). With age, there is increasing aberration in these processes leading to chronicity of injury and tissue fibrosis. Despite substantial research advances (*53*, *54*), lung transplantation remains the only treatment for advanced disease (*53*, *54*). Critical gaps persist in understanding the fine interplay between aging structural and immune cells that determines the fate of an injured lung. Here, we investigated the impact of hematopoietic age on lung fibrosis by decoupling it from the aging lung tissue. We found that, irrespective of the lung tissue or tissue-resident cell age, bone marrow age determines Mo-AM influx and fibrosis severity. Exacerbated fibrosis in recipients of aged bone marrow was not only associated with increased Mo-AM numbers but also fueled by a delayed transition of inflammatory, profibrotic Mo-AMs into a tissue-resident homeostatic state. We found that T_{reg}-derived IL-10 was a key factor that dampens pro-inflammatory Mo-AMs upon lung injury and that this axis was hampered with age.

Bone marrow–derived Mo-AMs are key drivers of lung fibrosis (*15*, *16*, *20*, *55*), with Mo-AM–like, scar-associated macrophages of monocytic origin observed to cluster around fibrotic foci in the lungs of patients with IPF (*56*). In models of bleomycin- and asbestos-induced fibrosis (*25*), the increased presence of Mo-AMs in fibrosis-susceptible, aged mice has been explained by age-related dysregulation

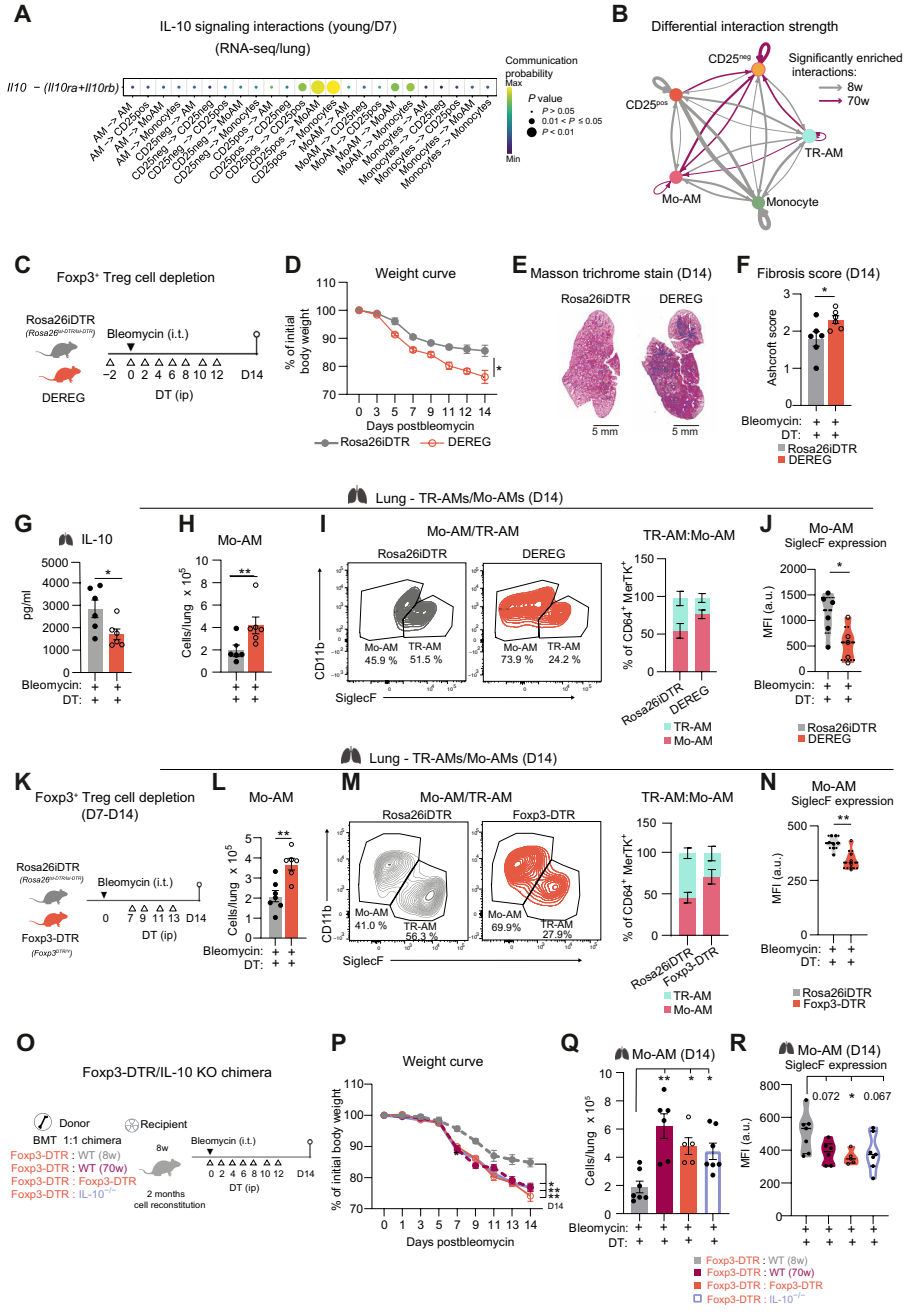

Fig. 6. IL-10–producing T_{regs} promote Mo-AM maturation and attenuate fibrosis. (**A** and **B**) CellChat analysis from transcriptomic data of sorted lung cell populations: TR-AMs, Mo-AMs, monocytes, $CD4^+$ $CD25^+$, and $CD4^+$ $CD25^-$ T cells from recipients of 8w or 70w bone marrow (D7/postbleomycin). (A) Receptor-ligand interactions of IL-10 signaling pathway from recipients of 8w bone marrow. (B) Differential interaction strength between the given cell types. Enriched interactions: gray (8w) and purple (70w). Arrow direction: interaction flow. Arrow weight: interaction strength. (**C**) Experimental setup for (**D** to **J**). DEREG mice or Rosa26iDTR (*Rosa26*$^{lsl\text{-}DTR/lsl\text{-}DTR}$) controls were given DT intraperitoneally (i.p) and bleomycin (intratracheally) at specified time points ($n = 6$ or 7 per group). (D) Body weight curve until D14. (E) Histological lung sections: Masson trichrome stain. (F) Modified Ashcroft fibrosis score of lung histology at D14 postbleomycin. (G) IL-10 levels from lung homogenates (ELISA). (H) Absolute numbers of lung Mo-AMs. (I) Representative flow cytometry plots and TR-AMs and Mo-AMs expressed as a percentage of $MerTK^+$ $CD64^+$ cells. (J) Mean fluorescence intensity of SiglecF expression on Mo-AMs. (**K**) Experimental setup for (**L** to **N**). Foxp3-DTR (*Foxp3*$^{DTR/Y}$) or Rosa26iDTR (*Rosa26*$^{lsl\text{-}DTR/lsl\text{-}DTR}$) mice were given bleomycin (intratracheally; D0) and DT (intraperitoneally) from D7 until D14 (end point) every 2 days. (L) Absolute cell numbers of lung Mo-AMs. (M) Representative flow cytometry plots and TR-AMs and Mo-AMs expressed as a percentage of $MerTK^+$ $CD64^+$ cells. (N) Mean fluorescence intensity of SiglecF expression on Mo-AMs. (**O**) Experimental setup for (**P** to **R**). Eight-week-old mice were irradiated and transplanted a 1:1 ratio of bone marrow cells: [Foxp3-DTR: WT (8w)]; [Foxp3-DTR: WT (70w)]; (Foxp3-DTR:Foxp3-DTR); (Foxp3-DTR: IL-$10^{-/-}$), challenged with bleomycin (intratracheally; D0) 2 months posttransplant, and administered DT every 2 days from D0 until D14 (end point). (P) Body weight curve. (Q) Absolute cell counts of lung Mo-AMs (D14). (R) Mean fluorescence intensity of SiglecF expression on Mo-AMs. Data are representative of one or two independent experiments. [(D) and (P)] Two-way ANOVA Tukey's post hoc multiple comparison test and [(F) to (N)] Student's two-tailed *t* test were used. For (Q) and (R), one-way ANOVA with post hoc Dunnett's multiple comparisons with the Foxp3-DTR:WT (8w) group as the control was used. Error bars represent SEM. $*P \leq 0.05$; $**P < 0.01$; n.s., not significant.

of epithelial cell differentiation and increased epithelial barrier permeability (*25*). However, this is based on studies conducted in naturally aged mice, where age-related aberrations in all cell compartments simultaneously manifest. Here, using heterochronic transplantation, we disentangled age-related effects of lung structural cells from those of bone marrow–derived immune cells. We observed that young mice receiving aged bone marrow exhibited an influx of Mo-AMs comparable to naturally aged mice upon bleomycin injury, and this was reversed when aged mice received young bone marrow.

Similar to naturally aged mice (*20*), young recipients of aged bone marrow had fewer TR-AMs at baseline. Inadequate self-maintenance by aged resident macrophages could lead to their increased substitution by bone marrow–derived macrophages over time. This is supported by recent findings showing progressive replacement of fetal macrophages with bone marrow–derived macrophages during aging in naive mice (*13*). The macrophage-niche model underscores niche availability as a core prerequisite for monocyte engraftment and differentiation to macrophages (*57*). Our findings using the thoracic shielding model indicate that, although niche space may influence monocyte/Mo-AM turnover under homeostasis, its sole availability does not explain the heightened monocyte/Mo-AM infiltration observed in recipients of aged bone marrow after bleomycin injury given similar numbers of host-derived tissue resident macrophages. In 1:1 bone marrow chimeras, aged Mo-AMs outcompeted young cells, suggesting that the influx is driven by the output, differentiation, or homing potential of aged bone marrow progenitors, independent of the lung resident cell niche. Although our study focuses on the transition phase of Mo-AMs as they start adopting a TR-AM–like fate, the aged bone marrow could already have an impact on monocyte function and transition, which warrants further work.

Restoring barrier integrity postinjury is a critical step and involves the differentiation of alveolar type 2 (AT2) cells into alveolar type 1 (AT1) cells, which are crucial for gas exchange (*58*). We found that repopulation of the lung with aged immune cells, while inducing heightened inflammation and cell infiltration to bleomycin-induced lung injury, did not alter the degree of initial injury to the lung tissue in the readouts we tested. A previous study mechanistically showed that early inflammatory signals from monocyte-derived macrophages in the lung were needed to prime AT2 cells for differentiation (*59*). However, prolonged activation led to the formation of a dysregulated intermediate cell state, hampering barrier repair (*59*, *60*). In line with this, we observed that young Mo-AMs exhibited an early inflammatory signature, which they promptly down-regulated and began differentiating into homeostatic TR-AMs. Conversely, aged Mo-AMs retained and exacerbated an inflammatory and profibrotic profile over time. We speculate that the failure of aged Mo-AMs to efficiently transition out of this early activated state contributes to impaired epithelial restoration and increased fibrosis with age.

The infiltration and subsequent differentiation of Mo-AMs are governed by signals present in the microenvironment, influencing their function and phenotype. We observed a heightened inflammatory milieu with increased levels of IFN-γ and IL-6 but reduced IL-10 in the lungs of young mice engrafted with aged bone marrow, suggesting the lack of a key resolutory mediator. IL-10 has been shown to play a regulatory role in fibrosis by limiting IL-17A–driven fibrotic pathology and reducing profibrotic TGF-β activity (*61*). However, its effects can be context dependent (*37*). In our model, IL-10 functioned as an early anti-inflammatory mediator, mitigating the initial inflammatory signature of Mo-AMs in young bone marrow recipients. IL-10R signaling on macrophages has previously been shown to be crucial for maintaining mucosal homeostasis in the gut and preventing colitis by promoting the maintenance of anti-inflammatory macrophages (*62*, *63*), with IL-10R loss leading to the accumulation of immature inflammatory macrophages (*64*). Conversely, in the absence of immediate inflammation, the presence of IL-10 may push Mo-AMs into a state of repair overdrive and perpetuate the fibrotic response as previously reported (*65*). However, in line with our findings, IL-10RA was specifically expressed on profibrotic macrophages in the lungs of patients with IPF (*65*), underscoring a role for IL-10–dependent modulation of macrophage function during lung fibrosis.

Our work showed that reduced IL-10 in recipients of aged bone marrow was due to its decreased production by T_{regs}. The absence of T_{reg}-derived IL-10 or depletion of T_{regs} replicated the worsened fibrosis observed in young mice transplanted with aged bone marrow. T_{regs} modulate the immune environment by dampening inflammation and promoting tissue repair (*66*) and, similar to the impact of IL-10, can have a dual role in fibrogenesis. Although T_{regs} can promote fibroblast stimulation under noninflammatory conditions (*67*), they can be antifibrotic, restraining inflammation and subsequent fibrosis perpetuated by effector $CD4^+$ T cells as seen in *Aspergillus fumigatus* infection–induced fibrosis (*68*) or upon sterile silicon dioxide–induced lung injury (*67*). We found that T_{regs} and T cell–produced IL-10 shaped the myeloid cell response during bleomycin-induced fibrosis. Although IL-10 did not directly affect the early recruitment of Mo-AMs in the lungs, it did critically influence the maturation of profibrotic Mo-AMs into homeostatic tissue resident-like cells. Furthermore, depletion of T_{regs} specifically during the fibrotic development phase (D7 to D14) was sufficient to hamper appropriate Mo-AM maturation into a TR-AM phenotype. Our findings distinguish the early lung injury phase (D0 to D7) from the fibrotic development phase (D7 to D21) in the bleomycin model. Although the loss of IL-10 or T_{regs} during the early injury phase heightens inflammation and affects readouts such as body weight loss, reducing IL-10 or T_{regs} during the fibrotic development phase drives the delayed transition of Mo-AMs without obvious effects on early inflammation.

T_{regs} from aged bone marrow recipients exhibited transcriptional alterations and showed a T_H1 skewing. In line with this, prior work found that aging leads to cell-intrinsic dysfunction in T_{regs}, impairing their ability to facilitate tissue repair in the lungs after influenza infection (*69*). We found that loss of IL-10 from T_{regs} alone, without significant reduction in their numbers, was sufficient to exacerbate disease severity and Mo-AM accumulation, highlighting that the loss of efficient IL-10 production by T_{regs} during aging leads to a dysfunctional resolutory circuit in the lungs. Although we focused on the role of T_{reg}-derived IL-10, Mo-AM maturation at different stages can be influenced by signals from other cell types, namely, group 2 ILCs (*70*, *71*) and basophils (*72*).

Together, our study highlights the overarching influence that the age of the hematopoietic system has on exacerbating lung fibrosis by promoting influx of Mo-AMs upon injury. By showing that the combination of increased numbers and stalled transition of Mo-AMs into a homeostatic state contributes to a worsened fibrotic outcome, we emphasize their crucial role in governing the tissue response to injury. Moreover, the identified T_{reg}-driven IL-10 axis, which we show hastens Mo-AM maturation and is suppressed by an aging bone

marrow, provides a promising therapeutic avenue to accelerate tissue repair and prevent the development of fibrosis.

MATERIALS AND METHODS

Study design

The aim of this study was to investigate the impact of an aging bone marrow on the development of lung fibrosis. In this study, we used bone marrow transplant models to generate chimeric mice in which young (8-week-old) mice were transplanted with cells from young (8-week-old) or aged (70-week-old) bone marrow, allowed to reconstitute for 2 months before intratracheal challenge with bleomycin to induce fibrosis. We explored the impact of the aging immune system on the course of lung fibrosis via bone marrow transplant, bone marrow chimeras, flow cytometry, lung histology, microscopy, enzyme-linked immunosorbent assay (ELISA)/LEGENDplex analysis, and readouts of weight loss and survival of the mice. We further studied the impact of IL-10 and interaction between cell types involved in an IL-10–mediated resolution axis via transcriptomic analysis and the use of transgenic mice. For most experiments, two to four independent replicate experiments, unless stated in the figure legends, were conducted, all of which yielded comparable results. Data shown in this study are representative of independent experiments as described in the individual figure legends. Sample sizes were in accordance with that specified in the study protocol for animal ethics; in most mouse experiments, a sample size of 4 to 12 (per group/time point/treatment) were determined to be needed to see a difference with a significance level of 5% and a statistical power of 0.8. The robust regression and outlier removal test (ROUT) ($Q = 1\%$) test was used to identify any outliers from the dataset. In addition, any data points excluded because of obvious technical errors are documented in data file S10. For most mouse experiments, a minimum of 5 to 10 mice per group per experiment were used in bleomycin groups and 4 to 6 mice in baseline (D0) or PBS control. Three mice per genotype were used as bone marrow donors per experiment, and cells from all donors per genotype were pooled before transplant into recipients. Histopathological scoring of lung sections was conducted by an independent blinded pathologist or automated quantification. Allocation of animals into experimental groups was random at the start of the experiment. Recipient mice of different bone marrow genotypes were housed within the same cage. The number of mice, replicate experiments, and statistical tests are provided in the respective figure legends.

Mice

All animal experiments performed in this study were carried out in accordance with current guidelines stipulated by the ethical review committee of the Medical University of Vienna and the Austrian Ministry of Sciences (protocol ID BMBWF-66.009/0338-V/Jb/2019; 2022-0.726.852; VL: 2023-0.684.562;). Healthy age-matched 8- to 10-week-old male mice (classified as young adult mice) and 70- to 80-week-old male mice (aged mice) were used throughout the study. C57BL/6J mice were originally purchased from Janvier Labs and bred in house at the Core Facility Laboratory Animal Breeding and Husbandry, Medical University of Vienna in a specific pathogen–free environment according to the Federation of European Laboratory Animal Science Associations (FELASA) guidelines. Only male mice were used throughout the study, both as recipients and bone marrow donors. All mice were matched for age and genetic background in individual experiments and fed a standard chow diet. Aged mice were housed in the same room as young mice. Within each bone marrow transplant experiment, each cage contained recipients from all groups/conditions of bone marrow donor cells to control for microbiome-derived effects. For further details on mouse strains, see Supplementary Materials and Methods.

Bleomycin administration

Mice were administered with bleomycin sulfate (Sigma-Aldrich) resuspended in 30 μl of endotoxin-free PBS (Sigma-Aldrich) at a dose of 1.5 U/kg (high dose, only used in Fig. 1F) or 1 U/kg (low dose, all other experiments) or with 30 μl of PBS only (controls) at D0 and harvested at days 7, 14, 21, or 42 postchallenge. Doses were calculated on the basis of the average weight of the mice before the start of the experiment. Mice were anesthetized via intraperitoneal injection of Ketasol (100 mg/kg; OGRIS Pharma) and Rompun (10 mg/kg; Bayer) and placed on a rodent intubation stand (BrainTree). The tongue was set aside with blunt ended forceps, and 30 μl of PBS or bleomycin sulfate was administered intratracheally using a 200-μl pipette. Animals were then placed on a heating pad and monitored until awake and ambulatory.

Bone marrow transplants

Whole-body irradiation was performed at 6 Gy twice (2 × 6 Gy) with a 3-hour gap between irradiation rounds. For thoracic shielding, lead shields were placed over the chest during irradiation at a single dose of 9 Gy. Bone marrow cells (4×10^6 cells) were harvested from young (8- to 10-week-old) and aged (70- to 75-week-old) ubiquitin C (UBC)–GFP, CD45.1 donors or 8- to 12-week-old TCR-$\alpha^{-/-}$, Foxp3-DTR, Rosa26DTR, and IL-$10^{-/-}$ mice and injected retro-orbitally in 100 μl of PBS, 4 hours postirradiation. For 1:1 bone marrow chimera, 2×10^6 cells from each genotype were mixed before administration. Mice were housed for 2 months posttransplantation for reconstitution before experiments. For a detailed protocol, see Supplementary Materials and Methods.

In vivo treatments

Eight- to 10-week-old WT (C57BL/6J) mice were administered 50 μl at a dose of 150 μg of anti–IL-10 (clone JES5.2A5) intranasally under light isoflurane anesthesia [2% isoflurane, O_2 (2 liters/min)] (D0 to D7 or D7 to D14, every alternate day) or anti-CD25 (clone PC6) at a dose of 500 μg per mouse per time point in 200 μl of PBS [D(−2) to D7 or D7 to D14, every alternate day]. DEREG mice received DT (50 μg/kg) intraperitoneally on D(−2), followed by 10 μg/kg every 2 days (D0 to D14); Foxp3-DTR mice received DT (10 μg/kg) intraperitoneally every 2 days from D0 to D14 or D7 to D14. Rosa26-DTR mice were used as controls for all experiments. Further details are in Supplementary Materials and Methods.

Cell isolation and organ processing

BALF, lungs, bone marrow, and blood were processed into single-cell suspensions for flow cytometry analysis, cell sorting, RNA-seq, or ex vivo culture. For the detailed protocol on organ processing, see Supplementary Materials and Methods.

Stimulation with PMA/ionomycin for intracellular IL-10 detection

Cell suspensions were resuspended in 100 μl of PBS and 1% bovine serum albumin (BSA) containing phorbol 12-myristate 13-acetate (PMA) (Sigma-Aldrich; 250 ng/ml) and ionomycin (Sigma-Aldrich; 1 μg/ml) and incubated at 37°C for 4 hours. Brefeldin-A (BioLegend; 1:1000 dilution) was added in the last hour. Cells were washed in cold PBS and 1% BSA, and extracellular and intracellular staining and fixing were conducted as described above.

Ex vivo IL-10 stimulation

Mo-AMs (defined as viable/CD45$^+$/CD64$^+$ MerTK$^+$/SiglecF^{lo}/CD11b$^+$ subset) were sorted from the lungs of young (8-week-old) and aged (70-week-old) mice 7 days after bleomycin treatment. Cells from four animals per groups per age were sorted and pooled together. From this pool, three wells, i.e., technical replicates of each age group, were seeded ex vivo on a 96-well plate at 50,000 cells per well in RPMI 1640 containing 3% fetal calf serum and 1% penicillin-streptomycin (Sigma-Aldrich) and stimulated with either murine IL-10 (eBioscience; 10 ng/ml) or GM-CSF (30 ng/ml, PeproTech) or control medium for 24 hours. The supernatant was collected for cytokine measurement by ELISA/LEGENDplex, and cells were lysed in TRIzol reagent (Invitrogen) for subsequent RNA isolation.

Histology

Lung tissue samples (the left lobe was taken from experiments without BAL collection) were fixed in 7.5% formalin overnight, embedded in paraffin, and sectioned (5 μm in thickness). Sections were stained with hematoxylin and eosin (H&E), Masson's trichrome (Sigma-Aldrich), α-SMA (Abcam), FoxP3 (D6O8R) rabbit monoclonal antibody (mAb) (Cell Signaling) followed by staining with 3,3'-diaminobenzidine tetrahydrochloride (DAB) substrate (SignalStain DAB substrate kit, Cell Signaling); F4/80 (D2S9R) XP rabbit mAb (Cell Signaling) followed by staining with Vector Red substrate kit, alkaline phosphatase (Vector Labs); and TUNEL (in situ cell death detection kit, TMR red, Roche) according to the manufacturer's guidelines.

Microscopy

Whole-section image scans were obtained using a Vectra Polaris microscope (PerkinElmer) or a TissueFAXS (TissueGnostics) at the Imaging Core Facility of the Medical University of Vienna. Images were assessed using QuPath software (version 3.0), TissueQuest (version 7.1), and HALO (version 3.6.4), and assessment parameters applied to whole-image scans and to all images within each experiment. For image quantification details, see Supplementary Materials and Methods.

Ashcroft score

Evaluation of the severity of fibrosis was performed by a blinded pathologist and done using the Ashcroft scoring system (*73*). Both H&E staining and Masson's trichrome staining were used for evaluation purposes. Each lung section was examined microscopically using a 10x objective. Fibrosis was assessed using a score ranging from 0 to 8 for each microscopic field based on the Ashcroft criteria, and the mean score was calculated.

Hydroxyproline measurement

Lung tissue samples were weighed and snap frozen before the hydroxyproline assay. The assay was conducted according to the manufacturer's instructions (Sigma-Aldrich, MAK463).

Cytokine and chemokine analysis

Tissue and serum cytokines/chemokines were measured using the LEGENDplex mouse macrophage/microglia panel (BioLegend), mouse TH panel (BioLegend), and mouse inflammation panel (BioLegend). Samples were prepared according to the manufacturer's protocols and analyzed by flow cytometry. Data analysis was performed using the LEGENDplex data analysis software. IL-10 (OPTeia mouse IL-10 ELISA, BD Biosciences) and TGF-β (Mouse TGF-beta 1 DuoSet ELISA, R&D Systems) were measured using ELISA following the manufacturer's instructions.

RNA isolation and quantitative PCR

mRNA was isolated with TRIzol reagent (Invitrogen) or RNeasy Mini and Micro kits (Qiagen). For real-time polymerase chain reaction (PCR) assays, cDNA synthesis was performed using the iScript cDNA Synthesis Kit (Bio-Rad), according to the manufacturer's protocol. Real-time PCR was performed with SYBR Green Master Mix reagents (Applied Biosystems) on a StepOnePlus real-time PCR system (Applied Biosystems). Transcript levels were normalized to *glyceraldehyde-3-phosphate dehydrogenase* (*Gapdh*).

Bulk RNA-seq (Quant-seq)

Lung immune cells from recipients of young and aged bone marrow (7 and 14 days postbleomycin) were sequenced using the QuantSeq 3′ mRNA-seq library prep kit FWD for Illumina (Lexogen). Sequencing was performed on an Illumina NovaSeq 6000. RNA-seq data were mapped to the GRCm39 (mm10) mouse genome using STAR v2.7.9a and analyzed for differential expression with limma-voom (limma v3.50.3). Normalized counts [$\log_2$(CPM), where CPM is counts per million] were used for downstream analysis, including PCA, cell-cell interaction (CellChat), and quality control. Further details on library preparation/bioinformatics analysis are in Supplementary Materials and Methods.

Single-cell RNA-seq

Single-cell RNA-seq was performed on BAL cells collected on day 7 after bleomycin challenge from four male, 8-week-old mice. Cells were processed and sequenced using the Chromium Next GEM single cell 3' reagent kits v3.1 on an Illumina HiSeq 4000. Data were aligned and processed with the CellRanger pipeline and analyzed using Seurat v4.1.1 in R v4.2.0. For further details, see Supplementary Materials and Methods.

Analysis of data from the HCLA

The HLCA v1.0 dataset was analyzed (*49*), using studies by Banovich and Kropski (2020), Kaminski (2020), Lafyatis Rojas (2019), Lambrechts (2021), Meyer (2019 and 2021), Misharin Budinger (2018), Wunderlink (2021), and Zhang (2021). Comparisons were made across lung conditions (healthy, COVID-19, and IPF) and age groups (young ≤40 years, aged >40 years) for cell types: classical monocytes (cMos), nonclassical monocytes (nMos), AMs, IMs, AM proliferating, CD4 T cells (T_H), and T_{regs}. Further details are provided in Supplementary Materials and Methods.

Statistical analysis

Data were analyzed using Prism (GraphPad Prism 8.0-10.2.3; GraphPad Software Inc., San Diego, CA) and are presented as means ± SD or means ± SEM (information for individual figures is in the corresponding figure legend). For comparisons between two groups,

Student's two-tailed *t* test, Mann-Whitney test, or multiple *t* tests followed by Holm-Šídák test was used. For comparison between multiple groups, a one-way (one treatment condition) or two-way analysis of variance (ANOVA) (two treatment conditions/different time points), followed by a Tukey's multiple comparison test, Dunnett's multiple comparison test, Šidák's multiple comparisons test, or a Bonferroni's multiple comparisons test (see figure legends) with a single pooled variance was used. A log-rank (Mantel-Cox) test was used for survival curves. Statistical significance: n.s., not significant; $*P < 0.05$, $**P < 0.01$, $***P < 0.001$, and $****P < 0.0001$. Statistical analysis for the RNA-seq analysis is presented in the Supplementary Materials and Methods.

Supplementary Materials

The PDF file includes:
Supplementary Materials and Methods
Figs. S1 to S11
Table S1
References (*74*–*86*)

Other Supplementary Material for this manuscript includes the following:
Data files S1 to S10
MDAR Reproducibility Checklist

REFERENCES AND NOTES

1. A. Bektas, S. H. Schurman, R. Sen, L. Ferrucci, Aging, inflammation and the environment. *Exp. Gerontol.* **105**, 10–18 (2018).
2. E. R. Fernandez Perez, C. E. Daniels, D. R. Schroeder, J. St Sauver, T. E. Hartman, B. J. Bartholmai, E. S. Yi, J. H. Ryu, Incidence, prevalence, and clinical course of idiopathic pulmonary fibrosis: A population-based study. *Chest* **137**, 129–137 (2010).
3. G. Raghu, D. Weycker, J. Edelsberg, W. Z. Bradford, G. Oster, Incidence and prevalence of idiopathic pulmonary fibrosis. *Am. J. Respir. Crit. Care Med.* **174**, 810–816 (2006).
4. T. A. Wynn, T. R. Ramalingam, Mechanisms of fibrosis: Therapeutic translation for fibrotic disease. *Nat. Med.* **18**, 1028–1040 (2012).
5. S. Meiners, O. Eickelberg, M. Königshoff, Hallmarks of the ageing lung. *Eur. Respir. J.* **45**, 807–827 (2015).
6. S. Gulati, V. J. Thannickal, The aging lung and idiopathic pulmonary fibrosis. *Am. J. Med. Sci.* **357**, 384–389 (2019).
7. J. M. Van Deursen, The role of senescent cells in ageing. *Nature* **509**, 439–446 (2014).
8. H. W. Stout-Delgado, S. J. Cho, S. G. Chu, D. N. Mitzel, J. Villalba, S. El-Chemaly, S. W. Ryter, A. M. K. Choi, I. O. Rosas, Age-dependent susceptibility to pulmonary fibrosis is associated with NLRP3 inflammasome activation. *Am. J. Respir. Cell Mol. Biol.* **55**, 252–263 (2016).
9. T. A. Wynn, K. M. Vannella, Macrophages in tissue repair, regeneration, and fibrosis. *Immunity* **44**, 450–462 (2016).
10. D. Hashimoto, A. Chow, C. Noizat, P. Teo, M. B. Beasley, M. Leboeuf, C. D. Becker, P. See, J. Price, D. Lucas, M. Greter, A. Mortha, S. W. Boyer, E. C. Forsberg, M. Tanaka, N. van Rooijen, A. García-Sastre, E. R. Stanley, F. Ginhoux, P. S. Frenette, M. Merad, Tissue-resident macrophages self-maintain locally throughout adult life with minimal contribution from circulating monocytes. *Immunity* **38**, 792–804 (2013).
11. L. van de Laar, W. Saelens, S. De Prijck, L. Martens, C. L. Scott, G. Van Isterdael, E. Hoffmann, R. Beyaert, Y. Saeys, B. N. Lambrecht, M. Guilliams, Yolk sac macrophages, fetal liver, and adult monocytes can colonize an empty niche and develop into functional tissue-resident macrophages. *Immunity* **44**, 755–768 (2016).
12. H. Aegerter, J. Kulikauskaite, S. Crotta, H. Patel, G. Kelly, E. M. Hessel, M. Mack, S. Beinke, A. Wack, Influenza-induced monocyte-derived alveolar macrophages confer prolonged antibacterial protection. *Nat. Immunol.* **21**, 145–157 (2020).
13. F. Li, F. Piattini, L. Pohlmeier, Q. Feng, H. Rehrauer, M. Kopf, Monocyte-derived alveolar macrophages autonomously determine severe outcome of respiratory viral infection. *Sci. Immunol.* **7**, eabj5761 (2022).
14. B. Machiels, M. Dourcy, X. Xiao, J. Javaux, C. Mesnil, C. Sabatel, D. Desmecht, F. Lallemand, P. Martinive, H. Hammad, M. Guilliams, B. Dewals, A. Vanderplasschen, B. N. Lambrecht, F. Bureau, L. Gillet, A gammaherpesvirus provides protection against allergic asthma by inducing the replacement of resident alveolar macrophages with regulatory monocytes. *Nat. Immunol.* **18**, 1310–1320 (2017).
15. A. V. Misharin, L. Morales-Nebreda, P. A. Reyfman, C. M. Cuda, J. M. Walter, A. C. McQuattie-Pimentel, C.-I. Chen, K. R. Anekalla, N. Joshi, K. J. N. Williams, H. Abdala-Valencia, T. J. Yacoub, M. Chi, S. Chiu, F. J. Gonzalez-Gonzalez, K. Gates, A. P. Lam, T. T. Nicholson, P. J. Homan, S. Soberanes, S. Dominguez, V. K. Morgan, R. Saber, A. Shaffer, M. Hinchcliff, S. A. Marshall, A. Bharat, S. Berdnikovs, S. M. Bhorade, E. T. Bartom, R. I. Morimoto, W. E. Balch, J. I. Sznajder, N. S. Chandel, G. M. Mutlu, M. Jain, C. J. Gottardi, B. D. Singer, K. M. Ridge, N. Bagheri, A. Shilatifard, G. R. S. Budinger, H. Perlman, Monocyte-derived alveolar macrophages drive lung fibrosis and persist in the lung over the life span. *J. Exp. Med.* **214**, 2387–2404 (2017).
16. N. Joshi, S. Watanabe, R. Verma, R. P. Jablonski, C.-I. Chen, P. Cheresh, N. S. Markov, P. A. Reyfman, A. C. Mc Quattie-Pimentel, L. Sichizya, Z. Lu, R. Piseaux-Aillon, D. Kirchenbuechler, A. S. Flozak, C. J. Gottardi, C. M. Cuda, H. Perlman, M. Jain, D. W. Kamp, G. R. S. Budinger, A. V. Misharin, A spatially restricted fibrotic niche in pulmonary fibrosis is sustained by M-CSF/M-CSFR signalling in monocyte-derived alveolar macrophages. *Eur. Respir. J.* **55**, 1900646 (2020).
17. A. J. Byrne, T. M. Maher, C. M. Lloyd, Pulmonary macrophages: A new therapeutic pathway in fibrosing lung disease? *Trends Mol. Med.* **22**, 303–316 (2016).
18. X. Zhou, R. A. Franklin, M. Adler, J. B. Jacox, W. Bailis, J. A. Shyer, R. A. Flavell, A. Mayo, U. Alon, R. Medzhitov, Circuit design features of a stable two-cell system. *Cell* **172**, 744–757.e17 (2018).
19. D. Aran, A. P. Looney, L. Liu, E. Wu, V. Fong, A. Hsu, S. Chak, R. P. Naikawadi, P. J. Wolters, A. R. Abate, A. J. Butte, M. Bhattacharya, Reference-based analysis of lung single-cell sequencing reveals a transitional profibrotic macrophage. *Nat. Immunol.* **20**, 163–172 (2019).
20. A. C. McQuattie-Pimentel, Z. Ren, N. Joshi, S. Watanabe, T. Stoeger, M. Chi, Z. Lu, L. Sichizya, R. P. Aillon, C.-I. Chen, S. Soberanes, Z. Chen, P. A. Reyfman, J. M. Walter, K. R. Anekalla, J. M. Davis, K. A. Helmin, C. E. Runyan, H. Abdala-Valencia, K. Nam, A. Y. Meliton, D. R. Winter, R. I. Morimoto, G. M. Mutlu, A. Bharat, H. Perlman, C. J. Gottardi, K. M. Ridge, N. S. Chandel, J. I. Sznajder, W. E. Balch, B. D. Singer, A. V. Misharin, G. R. S. Budinger, The lung microenvironment shapes a dysfunctional response of alveolar macrophages in aging. *J. Clin. Invest.* **131**, e140299 (2021).
21. Y. Lavin, D. Winter, R. Blecher-Gonen, E. David, H. Keren-Shaul, M. Merad, S. Jung, I. Amit, Tissue-resident macrophage enhancer landscapes are shaped by the local microenvironment. *Cell* **159**, 1312–1326 (2014).
22. S. Yona, K.-W. Kim, Y. Wolf, A. Mildner, D. Varol, M. Breker, D. Strauss-Ayali, S. Viukov, M. Guilliams, A. Misharin, D. A. Hume, H. Perlman, B. Malissen, E. Zelzer, S. Jung, Fate mapping reveals origins and dynamics of monocytes and tissue macrophages under homeostasis. *Immunity* **38**, 79–91 (2013).
23. J. Kulikauskaite, A. Wack, Teaching old dogs new tricks? The plasticity of lung alveolar macrophage subsets. *Trends Immunol.* **41**, 864–877 (2020).
24. L. Plantier, B. Crestani, S. E. Wert, M. Dehoux, B. Zweytick, A. Guenther, J. A. Whitsett, Ectopic respiratory epithelial cell differentiation in bronchiolised distal airspaces in idiopathic pulmonary fibrosis. *Thorax* **66**, 651–657 (2011).
25. S. Watanabe, N. S. Markov, Z. Lu, R. P. Aillon, S. Soberanes, C. E. Runyan, Z. Ren, R. A. Grant, M. Maciel, H. Abdala-Valencia, Y. Politanska, K. Nam, L. Sichizya, H. G. Kihshen, N. Joshi, A. C. McQuattie-Pimentel, K. A. Gruner, M. Jain, J. I. Sznajder, R. I. Morimoto, P. A. Reyfman, C. J. Gottardi, G. R. S. Budinger, A. V. Misharin, Resetting proteostasis with ISRIB promotes epithelial differentiation to attenuate pulmonary fibrosis. *Proc. Natl. Acad. Sci. U.S.A.* **118**, e2101100118 (2021).
26. C. Franceschi, M. Bonafè, S. Valensin, F. Olivieri, M. De Luca, E. Ottaviani, G. De Benedictis, Inflamm-aging. An evolutionary perspective on immunosenescence. *Ann. N. Y. Acad. Sci.* **908**, 244–254 (2000).
27. B. Dykstra, S. Olthof, J. Schreuder, M. Ritsema, G. de Haan, Clonal analysis reveals multiple functional defects of aged murine hematopoietic stem cells. *J. Exp. Med.* **208**, 2691–2703 (2011).
28. M. S. Kowalczyk, I. Tirosh, D. Heckl, T. N. Rao, A. Dixit, B. J. Haas, R. K. Schneider, A. J. Wagers, B. L. Ebert, A. Regev, Single-cell RNA-seq reveals changes in cell cycle and differentiation programs upon aging of hematopoietic stem cells. *Genome Res.* **25**, 1860–1872 (2015).
29. D. J. Rossi, D. Bryder, J. M. Zahn, H. Ahlenius, R. Sonu, A. J. Wagers, I. L. Weissman, Cell intrinsic alterations underlie hematopoietic stem cell aging. *Proc. Natl. Acad. Sci. U.S.A.* **102**, 9194–9199 (2005).
30. M. Mann, A. Mehta, C. G. de Boer, M. S. Kowalczyk, K. Lee, P. Haldeman, N. Rogel, A. R. Knecht, D. Farouq, A. Regev, D. Baltimore, Heterogeneous responses of hematopoietic stem cells to inflammatory stimuli are altered with age. *Cell Rep.* **25**, 2992–3005.e5 (2018).
31. K. Dorshkind, T. Hofer, E. Montecino-Rodriguez, P. D. Pioli, H.-R. Rodewald, Do haematopoietic stem cells age? *Nat. Rev. Immunol.* **20**, 196–202 (2020).
32. T. Tsukui, K.-H. Sun, J. B. Wetter, J. R. Wilson-Kanamori, L. A. Hazelwood, N. C. Henderson, T. S. Adams, J. C. Schupp, S. D. Poli, I. O. Rosas, N. Kaminski, M. A. Matthay, P. J. Wolters, D. Sheppard, Collagen-producing lung cell atlas identifies multiple subsets with distinct localization and relevance to fibrosis. *Nat. Commun.* **11**, 1920 (2020).
33. S. L. Vyalov, G. Gabbiani, Y. Kapanci, Rat alveolar myofibroblasts acquire alpha-smooth muscle actin expression during bleomycin-induced pulmonary fibrosis. *Am. J. Pathol.* **143**, 1754–1765 (1993).

34. E. L. Gautier, T. Shay, J. Miller, M. Greter, C. Jakubzick, S. Ivanov, J. Helft, A. Chow, K. G. Elpek, S. Gordonov, A. R. Mazloom, A. Ma'ayan, W.-J. Chua, T. H. Hansen, S. J. Turley, M. Merad, G. J. Randolph, Immunological Genome Consortium, Gene-expression profiles and transcriptional regulatory pathways that underlie the identity and diversity of mouse tissue macrophages. *Nat. Immunol.* **13**, 1118–1128 (2012).
35. C. Shi, M. Sakuma, T. Mooroka, A. Liscoe, H. Gao, K. J. Croce, A. Sharma, D. Kaplan, D. R. Greaves, Y. Wang, D. I. Simon, Down-regulation of the forkhead transcription factor Foxp1 is required for monocyte differentiation and macrophage function. *Blood* **112**, 4699–4711 (2008).
36. J. Gschwend, S. P. M. Sherman, F. Ridder, X. Feng, H.-E. Liang, R. M. Locksley, B. Becher, C. Schneider, Alveolar macrophages rely on GM-CSF from alveolar epithelial type 2 cells before and after birth. *J. Exp. Med.* **218**, e20210745 (2021).
37. H. Aegerter, B. N. Lambrecht, C. V. Jakubzick, Biology of lung macrophages in health and disease. *Immunity* **55**, 1564–1580 (2022).
38. P. P. Ogger, G. J. Albers, R. J. Hewitt, B. J. O'Sullivan, J. E. Powell, E. Calamita, P. Ghai, S. A. Walker, P. M. Erlean, P. Saunders, S. Kingston, P. L. Molyneaux, J. M. Halket, R. Gray, D. C. Chambers, T. M. Maher, C. M. Lloyd, A. J. Byrne, Itaconate controls the severity of pulmonary fibrosis. *Sci. Immunol.* **5**, eabc1884 (2020).
39. K. Atabai, S. Jame, N. Azhar, A. Kuo, M. Lam, W. M. Kleroy, G. Dehart, S. Rahman, D. D. Xia, A. C. Melton, P. Wolters, C. L. Emson, S. M. Turner, Z. Werb, D. Sheppard, Mfge8 diminishes the severity of tissue fibrosis in mice by binding and targeting collagen for uptake by macrophages. *J. Clin. Invest.* **119**, 3713–3722 (2009).
40. D. F. Fiorentino, A. Zlotnik, T. R. Mosmann, M. Howard, A. O'Garra, IL-10 inhibits cytokine production by activated macrophages. *J. Immunol.* **147**, 3815–3822 (1991).
41. E. Fraser, L. Denney, A. Antanaviciute, K. Blirando, C. Vuppusetty, Y. Zheng, E. Repapi, V. Iotchkova, S. Taylor, N. Ashley, V. S. Noble, R. Benamore, R. Hoyles, C. Clelland, J. M. D. Rastrick, C. S. Hardman, N. K. Alham, R. E. Rigby, A. Simmons, J. Rehwinkel, L.-P. Ho, Multi-modal characterization of monocytes in idiopathic pulmonary fibrosis reveals a primed type I interferon immune phenotype. *Front. Immunol.* **12**, 623430 (2021).
42. A. V. Misharin, L. Morales-Nebreda, G. M. Mutlu, G. R. S. Budinger, H. Perlman, Flow cytometric analysis of macrophages and dendritic cell subsets in the mouse lung. *Am. J. Respir. Cell Mol. Biol.* **49**, 503–510 (2013).
43. B. K. Weaver, E. Bohn, B. A. Judd, M. P. Gil, R. D. Schreiber, ABIN-3: A molecular basis for species divergence in interleukin-10-induced anti-inflammatory actions. *Mol. Cell. Biol.* **27**, 4603–4616 (2007).
44. A. P. Hutchins, S. Poulain, D. Miranda-Saavedra, Genome-wide analysis of STAT3 binding in vivo predicts effectors of the anti-inflammatory response in macrophages. *Blood* **119**, e110–e119 (2012).
45. C. Sabatel, C. Radermecker, L. Fievez, G. Paulissen, S. Chakarov, C. Fernandes, S. Olivier, M. Toussaint, D. Pirottin, X. Xiao, P. Quatresooz, J.-C. Sirard, D. Cataldo, L. Gillet, H. Bouabe, C. J. Desmet, F. Ginhoux, T. Marichal, F. Bureau, Exposure to bacterial CpG DNA protects from airway allergic inflammation by expanding regulatory lung interstitial macrophages. *Immunity* **46**, 457–473 (2017).
46. N. Gagliani, C. F. Magnani, S. Huber, M. E. Gianolini, M. Pala, P. Licona-Limon, B. Guo, D. R. Herbert, A. Bulfone, F. Trentini, C. D. Serio, R. Bacchetta, M. Andreani, L. Brockmann, S. Gregori, R. A. Flavell, M.-G. Roncarolo, Coexpression of CD49b and LAG-3 identifies human and mouse T regulatory type 1 cells. *Nat. Med.* **19**, 739–746 (2013).
47. N. Komatsu, S. Hori, Full restoration of peripheral Foxp3$^+$ regulatory T cell pool by radioresistant host cells in scurfy bone marrow chimeras. *Proc. Natl. Acad. Sci. U.S.A.* **104**, 8959–8964 (2007).
48. A. Liston, D. H. D. Gray, Homeostatic control of regulatory T cell diversity. *Nat. Rev. Immunol.* **14**, 154–165 (2014).
49. L. Sikkema, C. Ramírez-Suástegui, D. C. Strobl, T. E. Gillett, L. Zappia, E. Madissoon, N. S. Markov, L.-E. Zaragosi, Y. Ji, M. Ansari, M.-J. Arguel, L. Apperloo, M. Banchero, C. Bécavin, M. Berg, E. Chichelnitskiy, M.-I. Chung, A. Collin, A. C. A. Gay, J. Gote-Schniering, B. H. Kashani, K. Inecik, M. Jain, T. S. Kapellos, T. M. Kole, S. Leroy, C. H. Mayr, A. J. Oliver, M. von Papen, L. Peter, C. J. Taylor, T. Walzthoeni, C. Xu, L. T. Bui, C. De Donno, L. Dony, A. Faiz, M. Guo, A. J. Gutierrez, L. Heumos, N. Huang, I. L. Ibarra, N. D. Jackson, P. Kadur Lakshminarasimha Murthy, M. Lotfollahi, T. Tabib, C. Talavera-López, K. J. Travaglini, A. Wilbrey-Clark, K. B. Worlock, M. Yoshida, Lung Biological Network Consortium, M. van den Berge, Y. Bossé, T. J. Desai, O. Eickelberg, N. Kaminski, M. A. Krasnow, R. Lafyatis, M. Z. Nikolic, J. E. Powell, J. Rajagopal, M. Rojas, O. Rozenblatt-Rosen, M. A. Seibold, D. Sheppard, D. P. Shepherd, D. D. Sin, W. Timens, A. M. Tsankov, J. Whitsett, Y. Xu, N. E. Banovich, P. Barbry, T. E. Duong, C. S. Falk, K. B. Meyer, J. A. Kropski, D. Pe'er, H. B. Schiller, P. R. Tata, J. L. Schultze, S. A. Teichmann, A. V. Misharin, M. C. Nawijn, M. D. Luecken, F. J. Theis, An integrated cell atlas of the lung in health and disease. *Nat. Med.* **29**, 1563–1577 (2023).
50. C. Morse, T. Tabib, J. Sembrat, K. L. Buschur, H. T. Bittar, E. Valenzi, Y. Jiang, D. J. Kass, K. Gibson, W. Chen, A. Mora, P. V. Benos, M. Rojas, R. Lafyatis, Proliferating SPP1/MERTK-expressing macrophages in idiopathic pulmonary fibrosis. *Eur. Respir. J.* **54**, 1802441 (2019).
51. D. Wendisch, O. Dietrich, T. Mari, S. Von Stillfried, I. L. Ibarra, M. Mittermaier, C. Mache, R. L. Chua, R. Knoll, S. Timm, S. Brumhard, T. Krammer, H. Zauber, A. L. Hiller, A. Pascual-Reguant, R. Mothes, R. D. Bülow, J. Schulze, A. M. Leipold, S. Djudjaj, F. Erhard, R. Geffers, F. Pott, J. Kazmierski, J. Radke, P. Pergantis, K. Baßler, C. Conrad, A. C. Aschenbrenner, B. Sawitzki, M. Landthaler, E. Wyler, D. Horst, S. Hippenstiel, A. Hocke, F. L. Heppner, A. Uhrig, C. Garcia, F. Machleidt, S. Herold, S. Elezkurtaj, C. Thibeault, M. Witzenrath, C. Cochain, N. Suttorp, C. Drosten, C. Goffinet, F. Kurth, J. L. Schultze, H. Radbruch, M. Ochs, R. Eils, H. Müller-Redetzky, A. E. Hauser, M. D. Luecken, F. J. Theis, C. Conrad, T. Wolff, P. Boor, M. Selbach, A.-E. Saliba, L. E. Sander, SARS-CoV-2 infection triggers profibrotic macrophage responses and lung fibrosis. *Cell* **184**, 6243–6261.e27 (2021).
52. J. M. Kim, J. P. Rasmussen, A. Y. Rudensky, Regulatory T cells prevent catastrophic autoimmunity throughout the lifespan of mice. *Nat. Immunol.* **8**, 191–197 (2007).
53. T. E. King Jr., W. Z. Bradford, S. Castro-Bernardini, E. A. Fagan, I. Glaspole, M. K. Glassberg, E. Gorina, P. M. Hopkins, D. Kardatzke, L. Lancaster, D. J. Lederer, S. D. Nathan, C. A. Pereira, S. A. Sahn, R. Sussman, J. J. Swigris, P. W. Noble, ASCEND Study Group, A phase 3 trial of pirfenidone in patients with idiopathic pulmonary fibrosis. *N. Engl. J. Med.* **370**, 2083–2092 (2014).
54. L. Richeldi, R. M. du Bois, G. Raghu, A. Azuma, K. K. Brown, U. Costabel, V. Cottin, K. R. Flaherty, D. M. Hansell, Y. Inoue, D. S. Kim, M. Kolb, A. G. Nicholson, P. W. Noble, M. Selman, H. Taniguchi, M. Brun, F. Le Maulf, M. Girard, S. Stowasser, R. Schlenker-Herceg, B. Disse, H. R. Collard, INPULSIS Trial Investigators, Efficacy and safety of nintedanib in idiopathic pulmonary fibrosis. *N. Engl. J. Med.* **370**, 2071–2082 (2014).
55. L. Morales-Nebreda, A. V. Misharin, H. Perlman, G. R. Budinger, The heterogeneity of lung macrophages in the susceptibility to disease. *Eur. Respir. Rev.* **24**, 505–509 (2015).
56. T. Fabre, A. M. S. Barron, S. M. Christensen, S. Asano, K. Bound, M. P. Lech, M. H. Wadsworth II, X. Chen, C. Wang, J. Wang, J. McMahon, F. Schlerman, A. White, K. M. Kravarik, A. J. Fisher, L. A. Borthwick, K. M. Hart, N. C. Henderson, T. A. Wynn, K. Dower, Identification of a broadly fibrogenic macrophage subset induced by type 3 inflammation. *Sci. Immunol.* **8**, eadd8945 (2023).
57. M. Guilliams, G. R. Thierry, J. Bonnardel, M. Bajenoff, Establishment and maintenance of the macrophage niche. *Immunity* **52**, 434–451 (2020).
58. T. J. Desai, D. G. Brownfield, M. A. Krasnow, Alveolar progenitor and stem cells in lung development, renewal and cancer. *Nature* **507**, 190–194 (2014).
59. J. Choi, J.-E. Park, G. Tsagkogeorga, M. Yanagita, B.-K. Koo, N. Han, J.-H. Lee, Inflammatory signals induce AT2 cell-derived damage-associated transient progenitors that mediate alveolar regeneration. *Cell Stem Cell* **27**, 366–382.e7 (2020).
60. D. N. Kotton, E. E. Morrisey, Lung regeneration: Mechanisms, applications and emerging stem cell populations. *Nat. Med.* **20**, 822–832 (2014).
61. M. S. Wilson, S. K. Madala, T. R. Ramalingam, B. R. Gochuico, I. O. Rosas, A. W. Cheever, T. A. Wynn, Bleomycin and IL-1β–mediated pulmonary fibrosis is IL-17A dependent. *J. Exp. Med.* **207**, 535–552 (2010).
62. D. S. Shouval, A. Biswas, J. A. Goettel, K. M. Cann, E. Conaway, N. S. Redhu, I. D. Mascanfroni, Z. A. Adham, S. Lavoie, M. Ibourk, D. D. Nguyen, J. N. Samsom, J. C. Escher, R. Somech, B. Weiss, R. Beier, L. S. Conklin, C. L. Ebens, F. G. M. S. Santos, A. R. Ferreira, M. Sherlock, A. K. Bhan, W. Müller, J. R. Mora, F. J. Quintana, C. Klein, A. M. Muise, B. H. Horwitz, S. B. Snapper, Interleukin-10 receptor signaling in innate immune cells regulates mucosal immune tolerance and anti-inflammatory macrophage function. *Immunity* **40**, 706–719 (2014).
63. E. Zigmond, B. Bernshtein, G. Friedlander, S. Catherine, K.-W. Yona, O. Kim, R. Brenner, C. Krauthgamer, W. Varol, S. J. Müller, S. Jung, Macrophage-restricted interleukin-10 receptor deficiency, but not IL-10 deficiency, causes severe spontaneous colitis. *Immunity* **40**, 720–733 (2014).
64. I. Patik, N. S. Redhu, A. Eran, B. Bao, A. Nandy, Y. Tang, S. El Sayed, Z. Shen, J. Glickman, J. G. Fox, S. B. Snapper, B. H. Horwitz, The IL-10 receptor inhibits cell extrinsic signals necessary for STAT1-dependent macrophage accumulation during colitis. *Mucosal Immunol.* **16**, 233–249 (2023).
65. A. Bhattacharyya, K. Boostanpour, M. Bouzidi, L. Magee, T. Y. Chen, R. Wolters, P. Torre, S. K. Pillai, M. Bhattacharya, IL10 trains macrophage profibrotic function after lung injury. *Am. J. Physiol. Lung Cell. Mol. Physiol.* **322**, L495–L502 (2022).
66. N. Arpaia, J. A. Green, B. Moltedo, A. Arvey, S. Hemmers, S. Yuan, P. M. Treuting, A. Y. Rudensky, A distinct function of regulatory T cells in tissue protection. *Cell* **162**, 1078–1089 (2015).
67. S. Lo Re, M. Lecocq, F. Uwambayinema, Y. Yakoub, M. Delos, J. B. Demoulin, S. Lucas, T. Sparwasser, J.-C. Renauld, D. Lison, F. Huaux, Platelet-derived growth factor-producing CD4$^+$ Foxp3$^+$ regulatory T lymphocytes promote lung fibrosis. *Am. J. Respir. Crit. Care Med.* **184**, 1270–1281 (2011).
68. T. Ichikawa, K. Hirahara, K. Kokubo, M. Kiuchi, A. Aoki, Y. Morimoto, J. Kumagai, A. Onodera, N. Mato, D. J. Tumes, Y. Goto, K. Hagiwara, Y. Inagaki, T. Sparwasser, K. Tobe, T. Nakayama, CD103^{hi} T_{reg} cells constrain lung fibrosis induced by CD103^{lo} tissue-resident pathogenic CD4 T cells. *Nat. Immunol.* **20**, 1469–1480 (2019).

69. L. Morales-Nebreda, K. A. Helmin, M. A. Torres Acosta, N. S. Markov, J. Y. S. Hu, A. M. Joudi, R. Piseaux-Aillon, H. Abdala-Valencia, Y. Politanska, B. D. Singer, Aging imparts cell-autonomous dysfunction to regulatory T cells during recovery from influenza pneumonia. *JCI Insight* **6**, e141690 (2021).
70. S. Saluzzo, A. D. Gorki, B. M. J. Rana, R. Martins, S. Scanlon, P. Starkl, K. Lakovits, A. Hladik, A. Korosec, O. Sharif, J. M. Warszawska, H. Jolin, I. Mesteri, A. N. J. McKenzie, S. Knapp, First-breath-induced type 2 pathways shape the lung immune environment. *Cell Rep.* **18**, 1893–1905 (2017).
71. P. Loos, J. Baiwir, C. Maquet, J. Javaux, R. Sandor, F. Lallemand, T. Marichal, B. Machiels, L. Gillet, Dampening type 2 properties of group 2 innate lymphoid cells by a gammaherpesvirus infection reprograms alveolar macrophages. *Sci. Immunol.* **8**, eabl9041 (2023).
72. M. Cohen, A. Giladi, A. D. Gorki, D. G. Solodkin, M. Zada, A. Hladik, A. Miklosi, T. M. Salame, K. B. Halpern, E. David, S. Itzkovitz, T. Harkany, S. Knapp, I. Amit, Lung single-cell signaling interaction map reveals basophil role in macrophage imprinting. *Cell* **175**, 1031–1044. e18 (2018).
73. T. Ashcroft, J. M. Simpson, V. Timbrell, Simple method of estimating severity of pulmonary fibrosis on a numerical scale. *J. Clin. Pathol.* **41**, 467–470 (1988).
74. B. C. Schaefer, M. L. Schaefer, J. W. Kappler, P. Marrack, R. M. Kedl, Observation of antigen-dependent $CD8^+$ T-cell/dendritic cell interactions in vivo . *Cell. Immunol.* **214**, 110–122 (2001).
75. P. Mombaerts, A. R. Clarke, M. A. Rudnicki, J. Iacomini, S. Itohara, J. J. Lafaille, L. Wang, Y. Ichikawa, R. Jaenisch, M. L. Hooper, S. Tonegawa, Mutations in T-cell antigen receptor genes α and β block thymocyte development at different stages. *Nature* **360**, 225–231 (1992).
76. R. Kühn, J. Löhler, D. Rennick, K. Rajewsky, W. Müller, Interleukin-10-deficient mice develop chronic enterocolitis. *Cell* **75**, 263–274 (1993).
77. K. Lahl, C. Loddenkemper, C. Drouin, J. Freyer, J. Arnason, G. Eberl, A. Hamann, H. Wagner, J. Huehn, T. Sparwasser, Selective depletion of Foxp3+ regulatory T cells induces a scurfy-like disease. *J. Exp. Med.* **204**, 57–63 (2007).
78. T. Buch, F. L. Heppner, C. Tertilt, T. J. A. J. Heinen, M. Kremer, F. T. Wunderlich, S. Jung, A. Waisman, A Cre-inducible diphtheria toxin receptor mediates cell lineage ablation after toxin administration. *Nat. Methods* **2**, 419–426 (2005).
79. S. Jin, C. F. Guerrero-Juarez, L. Zhang, I. Chang, R. Ramos, C. H. Kuan, P. Myung, M. V. Plikus, Q. Nie, Inference and analysis of cell-cell communication using CellChat. *Nat. Commun.* **12**, 1088 (2021).
80. Y. Hao, S. Hao, E. Andersen-Nissen, W. M. Mauck, S. Zheng, A. Butler, M. J. Lee, A. J. Wilk, C. Darby, M. Zager, P. Hoffman, M. Stoeckius, E. Papalexi, E. P. Mimitou, J. Jain, A. Srivastava, T. Stuart, L. M. Fleming, B. Yeung, A. J. Rogers, J. M. McElrath, C. A. Blish, R. Gottardo, P. Smibert, R. Satija, Integrated analysis of multimodal single-cell data. *Cell* **184**, 3573–3587.e29 (2021).
81. C. Hafemeister, R. Satija, Normalization and variance stabilization of single-cell RNA-seq data using regularized negative binomial regression. *Genome Biol.* **20**, 296 (2019).
82. C. S. McGinnis, L. M. Murrow, Z. J. Gartner, DoubletFinder: Doublet detection in single-cell RNA sequencing data using artificial nearest neighbors. *Cell Syst.* **8**, 329–337.e4 (2019).
83. C. Domínguez Conde, C. Xu, L. B. Jarvis, D. B. Rainbow, S. B. Wells, T. Gomes, S. K. Howlett, O. Suchanek, K. Polanski, H. W. King, L. Mamanova, N. Huang, P. A. Szabo, L. Richardson, L. Bolt, E. S. Fasouli, K. T. Mahbubani, M. Prete, L. Tuck, N. Richoz, Z. K. Tuong, L. Campos, H. S. Mousa, E. J. Needham, S. Pritchard, T. Li, R. Elmentaite, J. Park, E. Rahmani, D. Chen, D. K. Menon, O. A. Bayraktar, L. K. James, K. B. Meyer, N. Yosef, M. R. Clatworthy, P. A. Sims, D. L. Farber, K. Saeb-Parsy, J. L. Jones, S. A. Teichmann, Cross-tissue immune cell analysis reveals tissue-specific features in humans. *Science* **376**, eabl5197 (2022).
84. R. Lopez, J. Regier, M. B. Cole, M. I. Jordan, N. Yosef, Deep generative modeling for single-cell transcriptomics. *Nat. Methods* **15**, 1053–1058 (2018).
85. M. D. Luecken, M. Büttner, K. Chaichoompu, A. Danese, M. Interlandi, M. F. Mueller, D. C. Strobl, L. Zappia, M. Dugas, M. Colomé-Tatché, F. J. Theis, Benchmarking atlas-level data integration in single-cell genomics. *Nat. Methods* **19**, 41–50 (2022).
86. J. W. Squair, M. Gautier, C. Kathe, M. A. Anderson, N. D. James, T. H. Hutson, R. Hudelle, T. Qaiser, K. J. E. Matson, Q. Barraud, A. J. Levine, G. La Manno, M. A. Skinnider, G. Courtine, Confronting false discoveries in single-cell differential expression. *Nat. Commun.* **12**, 5692 (2021).

Acknowledgments: We thank the Biomedical Sequencing Facility (CeMM and Medical University of Vienna), the Core Facilities Flow Cytometry and Imaging (Medical University of Vienna), and the staff of the Core Facility of Laboratory Animal Breeding and Husbandry (Medical University of Vienna). We thank P. Kuess for help with the thoracic shielding experiments. **Funding:** This work was supported by the Austrian Science Fund SFB-F061(P04) (S.K.) and Austrian Science Fund ZK 57-B and V 10 25-B (R.G.). **Author contributions:** Conceptualization: A.Fa., R.G., and S.K. Investigation (experimental): A.Fa., M.R., S.Z., L.P., A.Fo., A.Hl., K.L., J.B., F.M., F.O., F.Q., P.S., A.D.G., and R.G. Investigation (bioinformatics): F.D., A.Ha., and J.M. Funding acquisition: R.G. and S.K. Project administration: S.K. Resources: L.B., C.V., N.B., W.E., J.v.d.V., and C.C. Supervision: R.G. and S.K. Writing—original draft: A.Fa., R.G., and S.K. Writing—review and editing: all authors. **Competing interests:** The authors declare that they have no competing interests. **Data and materials availability:** RNA-seq data have been publicly deposited at the National Center for Biotechnology Information (NCBI) Gene Expression Omnibus (GEO) repository under accession numbers GSE274253 (bulk RNA-Seq) and GSE277799 (scRNA-seq). The subset of the HCLA (*49*) presented in this study was uploaded to Zenodo as Seurat and AnnData object. The CellTypist and consensus cell type annotation are stored in the respective metadata data slots—https://zenodo.org/records/14532104. No custom code was generated for this work; standard code was used as described in Materials and Methods. Tabulated data underlying the figures are provided in data file S10. All data needed to evaluate the conclusions in the paper are present in the paper or the Supplementary Materials.

Submitted 29 August 2023
Resubmitted 27 August 2024
Accepted 19 February 2025
Published 28 March 2025
10.1126/sciimmunol.adk5041